Siloxane Based Cellular Labeling:

Functional Applications in ^{1}H MRI

by

Alex Cusick

A Thesis Presented in Partial Fulfillment
of the Requirements for the Degree
Master of Science

Approved August 2014 by the
Graduate Supervisory Committee

Vikram Kodibagkar, Chair
Sarah Stabenfeldt
Jeff Kleim

ARIZONA STATE UNIVERSITY

December 2014

ABSTRACT

Modern medical conditions, including cancer, traumatic brain injury, and cardiovascular disease, have elicited the need for cell therapies. The ability to non-invasively track cells *in vivo* in order to evaluate these therapies and explore cell dynamics is necessary. Magnetic Resonance Imaging provides a platform to track cells as a non-invasive modality with superior resolution and soft tissue contrast. A new methodology for cellular labeling and imaging uses Nile Red doped hexamethyldisiloxane (HMDSO) nanoemulsions as dual modality (Magnetic Resonance Imaging/Fluorescence), dual-functional (oximetry/detection) nanoprobes. While Gadolinium chelates and super paramagnetic iron oxide-based particles have historically provided contrast enhancement in MRI, newer agents offer additional advantages. A technique using ^{1}H MRI in conjunction with an oxygen reporter molecule is one tool capable of providing these benefits, and can be used in neural progenitor cell and cancer cell studies. Proton Imaging of Siloxanes to Map Tissue Oxygenation Levels (PISTOL) provides the ability to track the polydimethylsiloxane (PDMS) labeled cells utilizing the duality of the nanoemulsions. ^{1}H MRI based labeling of neural stem cells and cancer cells was successfully demonstrated. Additionally, fluorescence labeling of the nanoprobes provided validation of the MRI data and could prove useful for quick *in vivo* verification and *ex vivo* validation for future studies.

ACKNOWLEGEMENTS

I would first like to take a moment to thank all of those who have helped me during this time of extensive learning and personal growth over the past two years.

I begin with my advisor, Dr. Vikram Kodibagkar, who has allowed me explore a unique avenue within Biomedical Engineering. Coming to Arizona State, I had an interest in trauma relating to the brain in hopes of pursuing a career related to contact sports (football, hockey, etc.). Dr. Kodibagkar went out of his way to provide me with a project that parlayed the use of Magnetic Resonance Imaging with applications directly relevant to traumatic brain injury and associated solutions. As a mentor, Dr. Kodibagkar always had an open door and ensured our lab was on the path to becoming experts in our field. He truly cares about the comprehensive answers to difficult research questions and made sure I was well informed to tackle anything thrown my way. Our group's lab meetings provided great practice to deal with holes being poked in our work as Dr. Kodibagkar made sure I knew how to defend and answer relevant questions. I will miss working is his lab, and have no doubt he is well on his way to becoming an imaging leader in the Valley and across the globe. Dr. Kodibagkar has provided me with unmatched experience across countless platforms (from clinical MR machines, to live animal work, to varied cell research), and for this, I am forever grateful.

Dr. Sarah Stabenfeldt has also been an unquestioned resource for me in my time at Arizona State. Her knowledge of neural injury and repair, neural tissue engineering, and regenerative medicine proved vital to my projects. Her door was also always open to any

questions I had regarding the crossover work between our labs. I am appreciative of all the time, resources, and energy her lab provided to my work specifically.

Her graduate student, and my peer, Caroline Addington was a critical part of my learning experience at Arizona State. Caroline was a pleasure to collaborate with and was intricate in expanding my biology-based knowledge. She demonstrated extraordinary patience in helping me grasp countless *in vitro* experiments related to neural stem cell work. Caroline is one of the most intelligent people I have ever been around, and I have no doubt her career in Biomedical Engineering will be very impactful.

I would also like to thank Dr. Jeff Kleim for serving on my committee. I had the privilege of being a member in Dr. Kleim's Neural Plasticity and Neurorehabilitation course and reveled in his all-encompassing look at modern neuroscience. Dr. Kleim took the theory behind the work and brought it to life through experimental examples. I consider myself very lucky to have him as a member of my committee and appreciate the time he has given to me.

The members of my lab were, perhaps, the biggest source of motivation and inspiration in the past two years of my life. Rohini Shankar was always there whenever I had any question related to MRI. She was consistently available to help me troubleshoot any research problems I had involving the scanner. Rohini is not only a special scientist, but also a special person. The bond we have formed is something I will always cherish and I will miss her dearly. I have no doubt she will be making a significant impact in the scientific community. The same could be said for Shubhangi Agarwal. Shubhangi was ready to help at any hour of any day when I had a question relating to our wet work. Her drive and passion for science is something to truly admire. I will miss her both in and out

of the lab, as she has been a great peer and friend, and am positive she will go on to do extraordinary work. The students who worked both alongside of me and allowed me to mentor them had a profound impact on my life. While I was teaching them, they were teaching me. For this, I am forever appreciative.

Lastly, I would like to thank anyone who has supported me over the past two years, specifically my family and friends. Research can be discouraging work, and so many people were there to pick me up every time I fell. The sacrifice of your time was an incredible blessing in my life. The entire Arizona State community was there for me throughout this process, and I am sorry to be leaving such a unique community. I look forward to watching the department and school continue to be a worldwide leader in biomedical research.

TABLE OF CONTENTS

Page

LIST OF FIGURES

CHAPTER 1

INTRODUCTION

1.1 Cellular Labeling and Nanoprobes

The complexity of modern disease, from degenerative and trauma-induced conditions to cancer, has elicited the need for cell therapies. One such cell treatment comes in the form of immunotherapy to target invading cancer cells. Antigens specific to cancer cells can be recognized as foreign by autologous immune cells, and manipulation of the host immune cells to sense the foreign antigens (amongst many "non-foreign" looking aspects of the cancer cells) has provided a specific, cell-based treatment [1]. In comparison to traditional chemotherapy and radiation therapy, this advantageous method can distinguish cancer cells from other rapidly growing cells for a more precise treatment. Similarly, stem cell therapies display the potential to treat disease via integration post-transplantation. For example, it has been shown that transplanting low doses of mouse embryonic stem cells into the rat striatum results in proliferation into fully differentiated fetal dopamine neurons in Parkinson's patients [2]. Parkinson's disease can be characterized by a decrease in dopaminergic neurons in the substantia nigra, and thus the stem cell therapy is beneficial. [3]

While these treatments are innovative and promising, definitive proof of safety and efficacy is needed for establishment as a clinical standard. Cell labeling and non-invasive tracking brings forth the ability to monitor cell dynamics *in vivo*, and evaluate the impact of cell therapies. Additionally, the ability to track cells *in vivo* offers many promising benefits throughout biomedical research.

Magnetic Resonance Imaging provides a powerful tool for the aforementioned applications due to superior soft tissue contrast and resolution. MRI utilizes the magnetic properties of nuclei for the visualization of biologic samples. The modality exploits the high sensitivity of the ^{1}H atom within the body from water, and to a lesser extent, lipid sources to non-invasively image endogenous structures and processes [4]. Exogenous contrast agents use the same magnetic properties to generate contrast in order to investigate multiple *in vivo* questions non-invasively (ie. cardiovascular performance, tumor detection in the brain, liver visualization) [5]. Recently, interest in these MRI contrast agents for molecular and cellular imaging applications has increased.

Traditionally, paramagnetic Gadolinium chelates and superparamagnetic iron oxide derived agents have been used for contrast enhancement. While these agents have historically provided contrast enhancement in MRI, newer agents offer additional advantages. One such technique utilizes perfluorocarbons (PFCs) as an oxygen reporter molecule in conjunction with ^{19}F MRI for monitoring of fluorinated compounds. Perfluorocarbons contain similar structure to organic compounds with a fluorine atom replacing hydrogen atoms in most cases [6]. An analogous technique using ^{1}H MRI was reported and is presented here. Proton Imaging of Siloxanes to Map Tissue Oxygenation Levels (PISTOL) provides the ability to track polydimethylsiloxane (PDMS) based nanoemulsions as MR contrast agents [7].

Gadolinium-based nanoparticles have been used for tumor cell labeling studies and display increased contrast on T1-weighted images [8]. Similarly, superparamagnetic iron oxide (SPIO) particles have been shown to successfully label immune cells and allow for tracking *in vivo* via contrast enhancement on T2-weighted images [9]. The particles created

from these two contrast agents are viable options for cell labeling and tracking; however, other options may provide additional function benefits. Newer methods also generate positive contrast without background signal – this contrast arises from no signal to positive signal whereas Gadolinium and iron oxide alter pre-existing signal.

^{19}F MRI focuses specifically on the resonance of fluorine allowing for images without the background of normal ^{1}H tissue. Anatomical information from ^{1}H MRI provides signal localization when overlaid with ^{19}F MRI. PFCs serve as oxygenation markers (reporting partial pressure of oxygen), and when combined with a fluorescent component, PFCs can be utilized as multi-functional nanoprobes [10].

HMDSO has also been shown as an oxygen reporter molecule (pO_2), and can be combined with a fluorescent component to create dual-modaility (MRI/Fluorescence), dual-functionality (oximetry/detection) nanoprobes for cellular and molecular imaging [11]. These methodologies utilize ^{1}H MRI and provide similar benefits to the PFCs used in conjunction with ^{19}F MRI. The siloxane selective sequences provide images without traditional ^{1}H MRI background signal through water and fat suppression (more detail in Chapter 1.4). ^{1}H MRI is more advantageous clinically than ^{19}F MRI due to the ability to acquire all images by exciting the ^{1}H proton at its resonance frequncy. ^{19}F MRI requires acquisition of signal from both ^{1}H excitation and ^{19}F excitation. This technology is currently not a part of established clinical scanners.

The aim of the project is to fabricate nanoemulsions capable of labeling and tracking cells using dual modality imaging – useful for quick *in vivo* verification and *ex vivo* validation – and focus on the different aspects of cell labeling applications. A novel mechanism utilizing siloxane-based nanoprobes to track cells could prove essential for the

treatment of a wide array of diseases. The added possibility of oximetry data using PISTOL is especially exciting for neural disease and cancer implications.

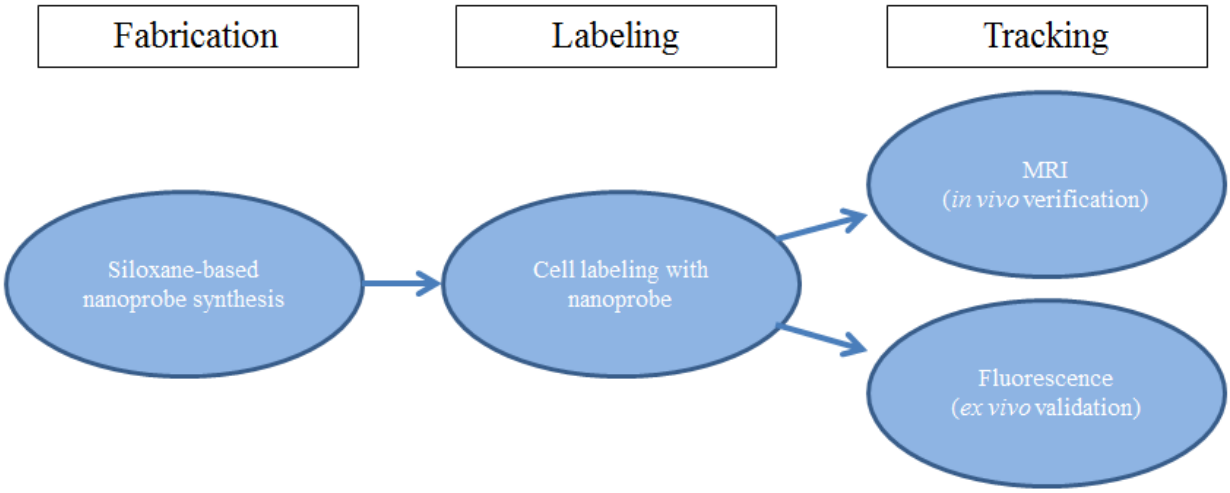

Figure 1.1 Outline for the Production of Dual-Modality, Dual-functionality Nanoprobes. Nanoprobe synthesis is followed by direct labeling of cells. Tracking can be achieved via *in vivo* MRI studies and validated with *ex vivo* fluorescence data.

1.2 Traumatic Brain Injury and Neural Stem Cells

A traumatic brain injury results from a bump, blow or jolt to the head or a penetrating head injury that interrupts normal function of the brain [12]. As the most common cause of death and disability in young people, TBI is graded as mild, moderate, or severe and can result in cognitive disorders and severe functional limitations [13]. The functional outcome of a TBI is influenced by neurological, physiological, and physical factors, and is heavily dependent on rehabilitation and early/late interventions for improved prognosis [14]. One such intervention with potential to improve functional outcome post-

TBI is cell-based therapies involving the transplantation of neural stem cells to the affected brain. This project will consider tracking transplanted neural stem cells following injury.

Transplantation of grafted neural stem cells presents a novel option to create a "biobridge" between uninjured tissue and the damage site in which grafted cells send migratory clues to endogenous neurogenic cells for enhanced repair mechanisms [15]. These results can be seen extensively in Tajiri et. al through immunohistochemistry, zymography, behavioral and neurological testing, and cell migration data.

Primary and secondary neuronal loss associated with traumatic brain injury can cause cognitive dysfunction. Significant cognitive improvement has been shown by the transplantation of neural stem cells in rats following traumatic brain injury [16]. Memory improvements and spatial learning increased as shown by the Morris Water Maze (MWM) tests [16]. Similarly, transplanted neural stem cells have been shown to survive, differentiate and improve motor function after traumatic brain injury [17]. Cell therapies to improve traumatic brain injury prognosis are promising, and the ability to track the cells to better understand the functional mechanisms underlying these improvements are necessary. Successful research on stem cell therapy presents an interesting opportunity for further analysis utilizing non-invasive, *in vivo* tracking methods allowing for data collection over multiple time points.

Magnetic Resonance Imaging has proven a powerful tool for neural stem cell tracking following transplantation. Gadolinium is not commonly used for labeling studies due to toxicity concerns and potential MR susceptibility issues when internalized by a cell[18]. Tracking path, migration and distribution is a valuable tool to optimize potential treatments and has been shown using superparamagnetic iron oxide particles to label neural

stem cells [19, 20]. ^{19}F MRI has also been used in conjuction with various perfluorocarbons to track neural stem cells *in vivo* [21, 22]. However, an existing clinical standard for cell tracking is absent, and further work should address this deficiency [19].

Here, the focus is on demonstrating and presenting successful neural stem cell labeling using fluorescence and MR imaging modalities. Additionally, ensuring maintained viability and functionality of the neural progenitor stem cells (NPSCs) post-labeling is of primary concern. Utilizing dual-modality, dual-functionality nanoprobes with ^{1}H MRI, an additional tool for NPSC tracking and improved treatment is presented.

1.3 Cancer Cell Applications

Magnetic Resonance-based labeling of cells has traditionally been used in various applications including cardiovascular disease, joint disease, aforementioned studies regarding the fate of stem cells in neurological disorders, and organ visualization [23]. And even though immune cells have been labeled for the treatment of cancer, only recently has interest arisen regarding paramagnetic labeling of cancer cells.

The process of cancer metastasis and tumor invasion has prompted the study of cancer cell migration patterns over long periods of time. Metastasis is a property of malignant cancer cells in which additional malignant cells are released from the primary tumor and disseminate to distant sites where they proliferate to form new tumors [24]. These metastases do not result from random cell survival, but rather by specialized subgroups of highly metastatic cells with specific properties beneficial to survival [24]. For this reason, along with the decreasing prognosis associated with metastatic tumors, it is beneficial to study the migration patterns of these malignant cells.

Again superparamagnetic iron oxide nanoparticles have been show effective for labeling and long-term cancer cell migration studies [25]. However, many important considerations must be taken into account when evaluating these studies over a significant period of time including viability, proliferation, cell division, stability and changes in relaxometry. The labeling agent must remain inert to allow the cell to exhibit its specific properties while still maintaining the quality of producing MR contrast. Labeling with SPIOs has also proven useful in studying mechanisms of metastasis and tumor dormancy through the evolution of a single cell subset, to tumor formation [26].

Extensive research has shown the efficacy of SPIOs in cell labeling. Specific to cancer cells, a similar labeling technique using siloxane-based nanoprobes could provide the additional benefit of functional oximetry.

Tumor hypoxia relates to vasculature and physiological conditions within the tumor and occurs when tumor cells are deprived of oxygen. Rapidly growing cancer cells outgrow their blood supply, and specific malignant cells have an unusual tolerance to limited oxygen availability [27]. These cells are found to alter their metabolism displaying excessive lactate production via aerobic glycolysis, and this increased lactate production is a characteristic associated with malignant cells [27, 28]. An association has also been established between tumor hypoxia and metastasis correlating to the “angiogenic switch” and an increasingly poor prognosis [28, 29].

In order to effectively apply treatment to tumor microenvironments, it would be advantageous to know which region of the tumor exhibits hypoxia. Additionally, the ability to measure hypoxia over time and at different treatment intervals provides a unique opportunity in evaluating cancer therapies as opposed to histological methods. PISTOL, in

unison with the siloxane-based nanoprobes, presents the additional functional benefit of oximetry. Thus, quantifying the pO_2 in the tumor microenvironment is an important aspect to tumor cell labeling.

Cancer spheroids bring forth an additional area of research susceptible to benefits from paramagnetic cell labeling. Tumor spheroids are multicellular structures grown in 3-dimensional culture to emulate the growth conditions and microenvironment of real tumors [30]. A renewed interest in tumor spheroids has emerged recently due to the flexibility as a therapeutically relevant model of *in vivo* tumors [31]. In this way, ineffective drug candidates can be eliminated before advancing into animal and human testing, and promising drugs – proving poor in 2D culture – can be identified and accelerated into testing [31]. Here, oximetry data would prove a valuable asset in helping identify drug performance and emphasizes the importance for cancer cell labeling in conjunction with dual-modality imaging.

1.4 Imaging Approach

1.4.1 MRI Principles

At the foundation of MRI signal generation is a fundamental property of atomic nuclei called spin. While the actual phenomenon is quantum mechanical in nature, each nuclei has an intrinsic angular momentum giving rise to a magnetic moment. Spin can exist in an "up" or "down" state and behaves like a tiny magnet in the presence of an external magnetic field. However, without the presence of an external magnetic field, these spin states are indistinguishable.

In terms of generating NMR signal, only nuclei with a net overall spin are of concern (ie. ^{1}H and ^{19}F as mentioned with regards to labeling). In the presence of an external magnetic field, known as B_0, the nuclei will align in their distinguishable "up" and "down" states. At room temperature, the number of spins aligning in the "up" (higher energy) orientation slightly outnumber the number of spins aligning in the "down" (lower energy) orientation. This relationship is governed by Boltzman statistics as shown below

$$N^-/N^+ = e^{-E/kT} \qquad [1]$$

Where N^- is the number of spins in the lower energy state, N^+ is the number of spins in the higher energy state, E is the energy difference between spin states, k is the Boltzmann constant (1.3805x10-23 J/Kelvin), and T is the temperature in Kelvin.

At this point, it is necessary to introduce the classical vector model which assumes a net magnetization in a bulk, macroscopic view. The higher energy spins align along the direction of the external magnetic field and outnumber the lower energy spins creating a net magnetization known as M_0.

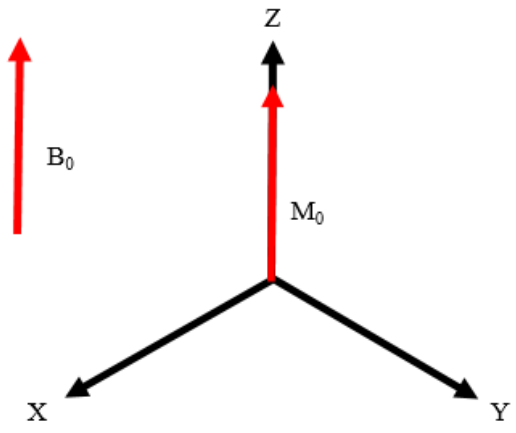

Figure 1.2 Higher Energy Spins Align in the Direction of the Applied Magnetic Field. A net magnetic field (M_0) is generated along the Z-axis in same direction as external magnetic field (B_0).

In order to generate NMR signal, voltage must be produced by a varying magnetic field, and this process is governed by Faraday's Law of induction.

$$V = -N(d\phi/dt) \quad [2]$$

This change in magnetic flux over time induces a time-varying voltage in a coil, but generating a varying magnetic field requires transverse magnetization.

The magnetic moment of the bulk magnetization (M_0) is precessing around B_0 at a specific frequency known as Larmor frequency. Larmor frequency is dependent on static field strength and governed by the following equation…

$$B_0(\gamma) = \omega \quad [3]$$

Where B_0 is the magnetic field strength (Tesla), γ is the gyromagnetic ratio (nuclei dependent) and ω is the Larmor frequency.

By taking the bulk magnetization along the Z-axis and tipping it into the transverse plane, voltage can be generated by the varying magnetic field as M_0 precesses around B_0. The perturbation of the bulk magnetization at equilibrium is known as excitation and can be accomplished with an external radio frequency (RF) magnetic field known as B_1. Resonance is achieved when the frequency of the B_1 RF pulse matches Larmor frequency – also matching the frequency of the static B_0 field. The flip angle determines the amount of magnetization flipped into the transvers (XY) plane and is governed by…

$$\Theta = \gamma \int_0^{T_p} B_1 \, dt \quad [4]$$

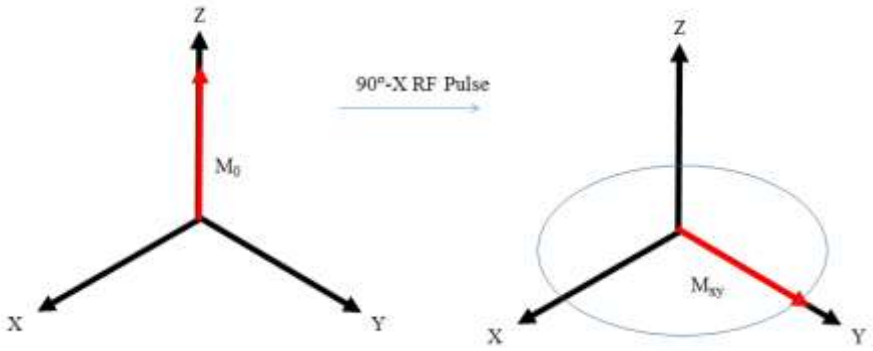

Figure 1.3 The B_1 Magnetic Field Flips the Net Magnetization into the Transverse Plane. A 90º RF pulse along the X axis flips M_0 into the XY-plane allowing for current generation.

The time during which the B_1 field is turned on determines the flip angle, and when turned off, the nuclear spins return to align along the static magnetic field. The process is known as relaxation and occurs as a longitudinal and transverse component.

The time constant which describes how the magnetization returns to equilibrium along the Z-axis (longitudinal) is known as T_1 or spin-lattice relaxation time. The longitudinal relaxation rate, R_1, has an inverse relationship with T_1. T_1 is governed by the following equation…

$$M_z = M_0 (1 - e^{-t/T1}) \qquad [5]$$

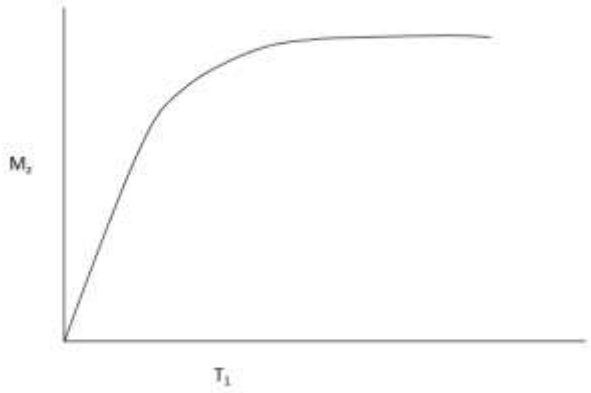

Figure 1.4 Schematic of an Exemplary T_1 Recovery Curve. Longitudinal magnetization tends to grow with time constant T_1.

The time constant which describes how the magnetization returns to equilibrium in the XY-plane (transverse) is known as T_2 or spin-spin relaxation time. The transverse relaxation rate, R_2, has an inverse relationship with T_2. T_2 is governed by the following equation…

$$M_{xy} = M_0 (e^{-t/T2}) \quad [6]$$

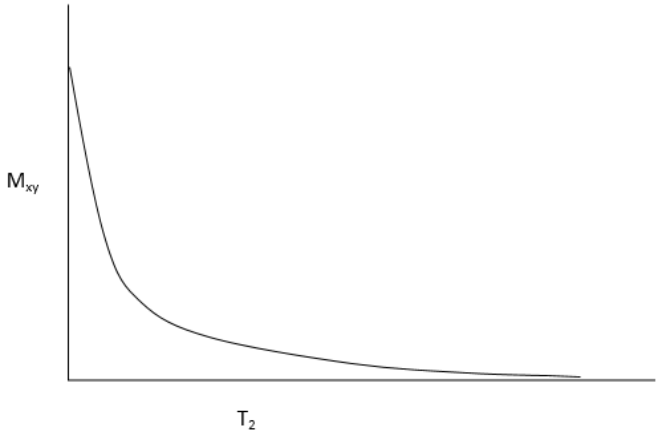

Figure 1.5 Schematic of an Exemplary T_2 Decay Curve. Transverse magnetization tends to decay with time constant T_2.

In conjunction with the B_1 field, magnetic field gradients are used (G_x, G_y, G_z) for more specific excitation and are the key behind pulse sequence programming.

1.4.2 Siloxane Selectivity

As the transverse magnetic field precesses around the Z-axis, a current is induced in a coil of wire located around the X-axis. A sine wave is produced by plotting this current as a function of time, and this signal is known as Free Induction Decay (FID). The magnetic field gradients are employed in a way allowing for the acquisition of the FID. With the help of the Fourier Transform, this signal can be converted into the frequency domain and aid in siloxane selectivity via the chemical shift phenomenon.

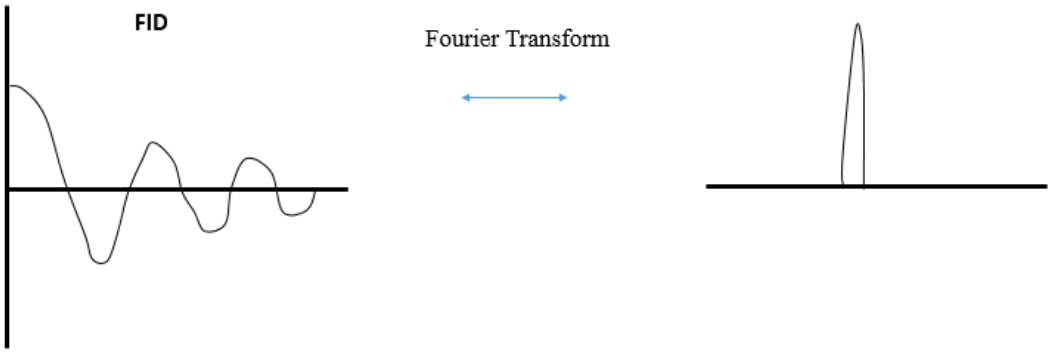

Figure 1.6 Free Induction Decay Schematic. FID (time domain) converted to the frequency domain using the Fourier Transform.

The FID carries information from multiple frequencies centered around the Larmor frequency due to chemical shift. Chemical shift is brought about because of inherent differences in the resonance frequency of precessing protons [32]. The phenomenon is caused by variations in electron density due to differences in types of nuclei and molecular bonding [32]. In other words, the FID contains information from excited ^{1}H protons, however, the precise resonant frequency will depend on the molecular structure and bonding of the ^{1}H atom to other atoms.

The chemical shift of a specific nucleus is measured as the difference between its resonance frequency and a standard. This property is measured in ppm and given the symbol δ.

$$\delta = [(\nu - \nu_{ref}) * 10^{6}]/ \nu_{ref} \quad [6]$$

Therefore, while water, fat, siloxane and other organic compounds will all contain ^{1}H, the chemical shift will be different for each. This information is used to create an NMR spectra where water falls at 4.7 ppm, fat falls at 1.0 ppm, and siloxane falls between -0.5 and 0.5.

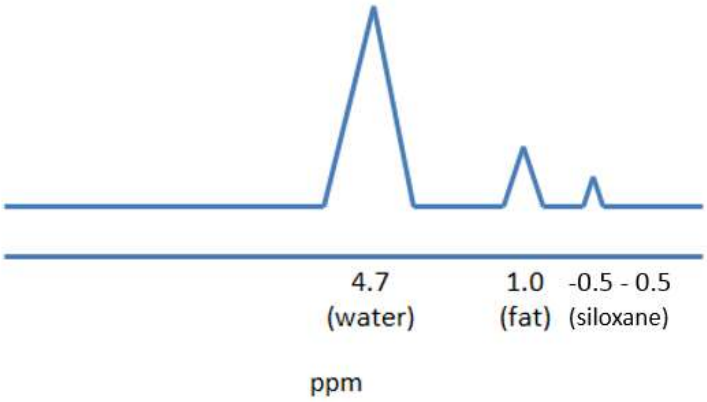

Figure 1.7 Example NMR Spectra from Acquisition of Sample Containing Water, Fat and Siloxane. Each hydrogen-containing molecule resonates at a specific frequency (water at 4.7 ppm, fat at 1.0 ppm, and siloxane at 0.5 to -0.5 ppm) with respect to a standard.

The nanoprobes used for cell labeling are able to generate signal without the background ^{1}H signal due to chemical shift. Proton imaging of siloxanes to map tissue oxygenation levels (PISTOL) employs a chemical-shift selective (CHESS) spin echo sequence to locate hexamethyldisiloxane (HMDSO) [33]. This sequence provides optional water and fat suppression along with a long echo time (>50 ms) for additional fat suppression [33]. T_1 mapping can quantify pO_2 and provide functional oximetry essential to the nanoprobes as discussed further in Chapter 3.

1.4.3 Fluorescence

The second modality utilized by the siloxane-based nanoprobes is fluorescence imaging for detection and *ex vivo* verification. While the modality requires penetration of light at depths unsuited for most *in vivo* studies, the cost effective nature, easy handling and lack of radioactivity in fluorescent tools has renewed interest via implementation with other modalities [34]. Optical fluorescence has been shown to aid in imaging of specific

tumor-associated molecular targets and is a promising tool for integration with multiple imaging systems [35].

A fluorophore is a fluorescent chemical compound capable of absorbing energy and re-emitting light of a specific wavelength upon light excitation [36]. Each fluorophore has an excitation and emission spectra.

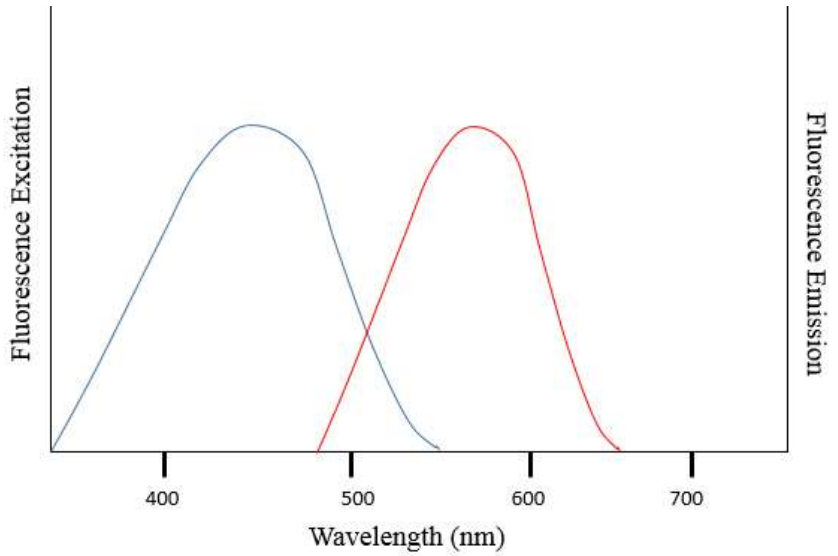

Figure 1.8 Example Excitation/Emission Spectra of Undefined Fluorophore. The excitation bandwidth (peak near 450 nm) and emission bandwidth (peak near 575 nm) allow for light detection of a specific fluorophore.

CHAPTER 2

NANOPARTICLE FABRICATION AND CELL TESTING

2.1 Nanoparticle characterization

An effective way to synthesize siloxane-based nanoparticles has been discussed in depth [7,11]. Nanoemulsions can be used as delivery vehicles for imaging agents in order to monitor dynamic *in vivo* processes [37]. The emulsifying agent contains two distinct regions, and can be characterized as amphiphillic (having both hydrophilic and lipophilic parts). This characteristic of the emulsifier provides an excellent opportunity for particle loading and fabrication. The hydrophilic head will tend to shield the lipophilic tail from water and thus internalize a selected delivery agent [38]. For the following experiments, polydimethylsiloxane (PDMS) and a fluorescent component were chosen as the "center" of the nanoparticles for contrast and functional imaging upon integration with cells. Sonication -- another vital step in the fabrication process – involves using high energy sound waves to increase even dispersion of nano-sized particles [39]. Filtration following sonication increases uniformity amongst particle sizes and gives partial control of particle diameter.

The following schematic illustrates the nanoprobe fabrication process and a specific methodology is presented shortly thereafter.

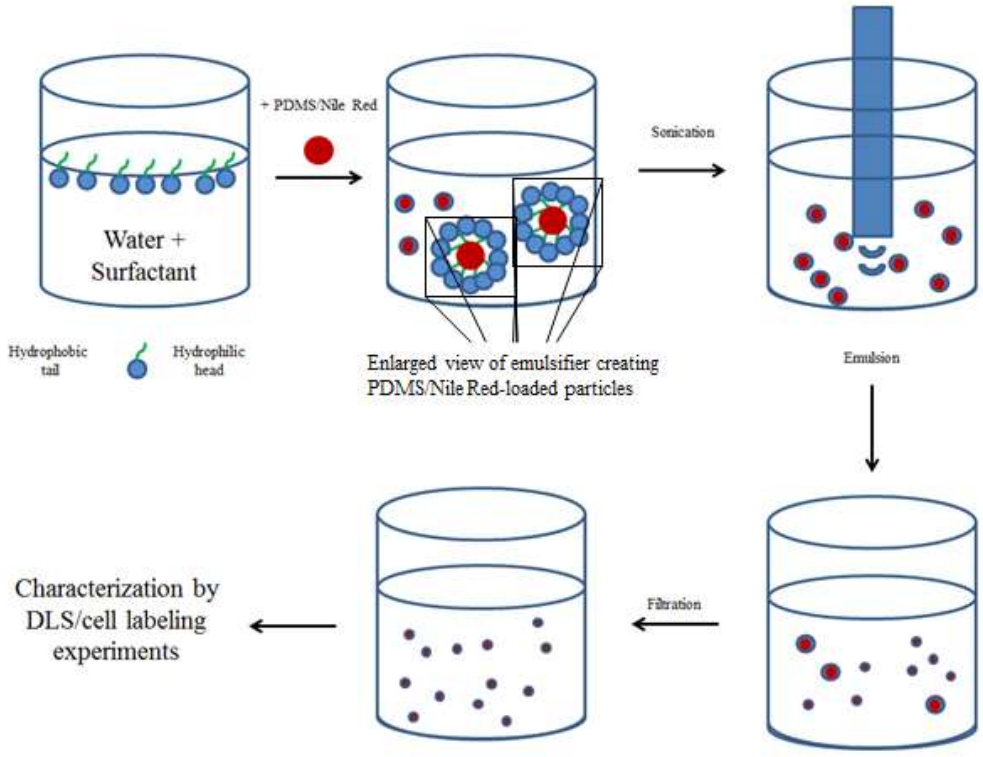

Figure 2.1 Nanoprobe Fabrication Process of PDMS/Nile Red-loaded Emulsions. Emulsifier with hydrophobic head and hydrophilic tail encapsulates PDMS/Nile Red to limit interaction between water and tail (repelled by water).

Nanoprobe synthesis occured at 70°C and particle composition was as follows, 55% deionized water, 40% siloxane, and 5% surfactant (emulsifying agent). Deionized water was attained from Arizona State University laboratory facilities. Previous fabrication experiments utilized HMDSO. For all labeling experiments, PDMS (Alfa Aesar, Ward Hill, Massachusetts, USA) with a molecular weight of 410 g/mol was utilized in place of HMDSO. The factors influencing this decision are discussed (Page 20). Solutol® HS 15, received as a gift from the BASF Corporation (Florham Park, New Jersey,USA), was used as the emulsifying agent. Two different fluorophores (Nile Red and Rhodamine B) were

used in emulsion synthesis, and their roles are discussed shortly. Emulsion batches were made in various batch volumes (most commonly 2 mL, 5mL, and 10 mL). Batches containing Nile Red were made in 5 mL volumes, while batches containing Rhodamine B were made in 2 mL volumes for conservation of resources.

Initially, HS 15 was heated and transitioned from a solid to liquid state within a 20mL scintillation vial (Sigma-Aldrich; St. Louis, Missouri, USA). Deionized water was measured out accordingly and placed in a vial. This vial was placed on a heat/stir plate within a water bath. After the system reached 70°C, as measured by a temperature probe, HS 15 (in liquid state) was added to deionized water and allowed to mix for 2 minutes.

- While mixing occurred, PDMS and a fluorophore were combined via two different methodologies. For Nile Red (Fisher Scientific; Waltham, Massachusetts, USA), ethanol was used to dissolve Nile Red at a ratio of 3.9 mg/mL. Once dissolved, Nile Red/ethanol was added to PDMS at a volume resulting in 0.1mM final Nile Red dye concentration in the emulsion. The dye was added on a heat/stir plate for 5 minutes at 70°C in an effort to force ethanol evaporation.
- For Rhodamine B, PE (Lissamine Rhodamine B) dissolved in chloroform was purchased from Avanti Polar Lipids, Inc (Alabaster, Alabama, USA). A proper volume to result in 0.1mM of Rhodamine in the final emulsion was measured and placed in a vial. Using a Rotovap (Buchi Corporation; Flawil, Switzerland), this compound was gently heated at 40°C for an hour. Following evaporation, Rhodamine was placed under a vacuum overnight to ensure the absence of chloroform. PDMS was then added to the chloroform-free Rhodamine.

The PDMS/fluorophore combination was added to the deionized water/surfactant mixture in a drop-by-drop fashion to allow for particle formation. The mixture was allowed to sit at 70°C for 15 minutes prior to sonication. Sonication occurred for a total of 45 minutes (3, 15 minute intervals) at 150W and a duty cycle of 50%, using an Omniruptor 4000 Ultrasonic Homogenizer (Omni International; Tulsa, Oklahoma, USA). The sample was de-bubbled and filtered with CELLTREAT (Celltreat Scientific; Shirly, Massachusetts, USA) 0.22µm syringe filters 10 times prior to particle size measurement. Nanoparticles were characterized using Delsa Nano Particle Size Analyzer (Beckman Coulter; Pasadena, CA, USA) through Dynamic Light Scattering (DLS).

Particle size typically ranged from 50nm – 150nm following sonication and filtration. Peak number average of particle diameter was taken from 8 samples with an average diameter found to be 98.24 ± 28.3 nm.

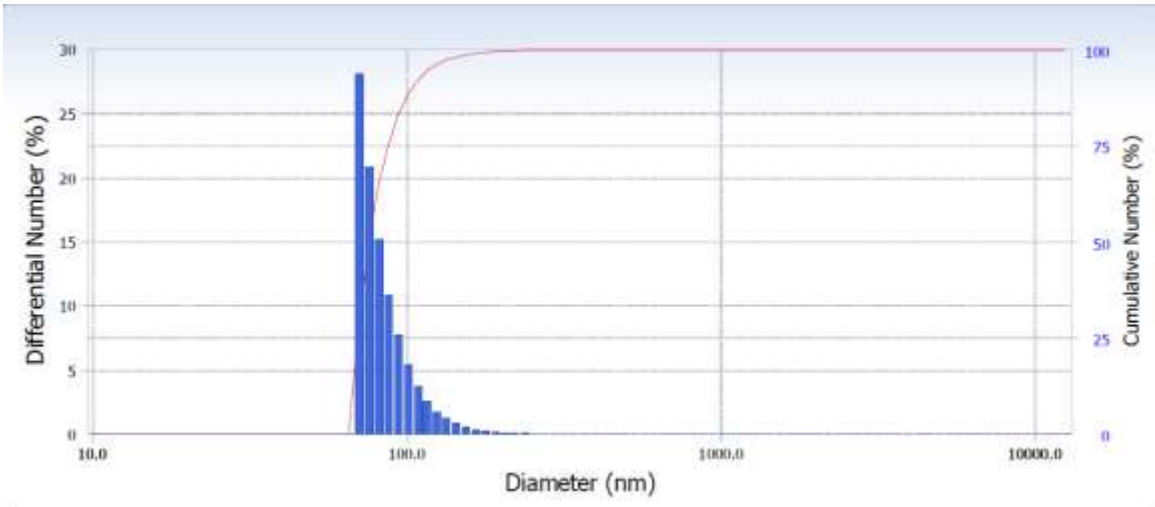

Figure 2.2 Number Average Measurement of Sample Size by Dynamic Light Scattering. Nanoparticle sample as measured by DLS with peak diameter number average of 84.9 ± 21.2.

These particles are used in a method of labeling known as direct labeling. This methodology is well-established and cost effective, with the pitfalls being signal decay over time with mitotic division [40]. There are three mechanisms by which the nanoparticles likely enter the cell: direct diffusion across the cell membrane, endocytosis, and transport across ion channels [41]. While labeling via the ion channels is highly unlikely, particle size and charge is an important aspect to consider when assuming the processes by which the cell is labeled. Loosely speaking, the smaller the particle size the better the odds to permeate the cell membrane. Thus, it is encouraging to see the particles formed at the nano-scale. A necessary study moving forward is characterizing the zeta potential of the particles. Understanding the electrokinetic potential of the nanoprobes would go a long way in better defining the mechanisms by which the cell becomes labeled.

The decision to use the heavier siloxane, PDMS, as opposed to the more traditionally used HMDSO in literature had to do with stability. HMDSO nanoparticles were found to undergo phase separation shortly after synthesis, whereas particles fabricated with PDMS did not separate remaining stable over longer periods of time. Additionally, nanoprobes were synthesized with both Nile Red and Rhodamine B. Nile Red was used as per the protocols of previous literature [11], but was found to cause toxicity in longer migration studies using neural stem cells (Chatper 2.2). For this reason, Rhodamine B was integrated into the particles and showed a decrease in long-term toxicity of neural stem cells. However, Rhodamine B proved more susceptible to photobleaching than Nile Red, and care was taken to preserve signal during experimentation.

2.2 Effects of labeling on NPSCs

[A special acknowledgement to Caroline Addington for NPSC harvest and maintenance, and figure]

2.2.1 NPSC harvest and maintenance

Neural progenitor stem cells were harvested from the medial and lateral germinal eminence of pups within the pregnant C57BL/6 mouse on the 14 and ½ day of pregnancy. Cells were placed in growth factor-embedded media and cultured in suspension. For optimal conditions, cells were used experimentally between passage No.'s 3 and 6.

Working NPSC media was created in 100mL batches. 94.3 mL of Dulbecco's Modified Eagle Medium (DMEM, Life Technologies; Carlsbad, CA, USA) was added to 2.0mL of glucose (6 ng/mL, Arcos Organics; Geel, Belgium)in deionized H_2O, 0.5 mL of HEPES buffer (5mM, Sigma-Aldrich), 0.1 mL of progesterone (62.9 ng/mL, Sigma-Aldrich), 1.0 mL of putrescine (9.6 µg/mL, Sigma-Aldrich), and 7.32 uL of Heparin (25 mg/mL, Sigma-Alrich). At this point, media filtration took place using a 0.22um PES Corning disposable vacuum filtration system (Fischer Scientific) to remove potential contaminants. Following filtration, 2.0 mL of B27 growth supplement (1X, Life Technologies), 0.2 mL of insulin (5 µg/mL, Sigma-Aldrich), 50µL of transferrin (5 µg/mL, Sigma-Aldrich), and 9.65 µL of sodium selenite (5 ng/m, Sigma-Aldrich). 20µL of Epidermal growth factor (EGF) (20 ng/mL, Sigma-Aldrich.) and 25µL of fibroblast growth factor (FGF) (5 ng/mL, Sigma-Aldrich) were added to the media to limit stem cell differentiation.

Neural stem cells were labeled with 10 µL of nanoparticles per 1.0 mL of working media for an incubation time of 1 hour. Following incubation, cells were lightly spun down and re-suspended (still in neurosphere form) using nanoparticle-free NPSC media. NPSCs were labeled in "neurosphere" form as shown below. At this point, labeled cells were used in various experiments.

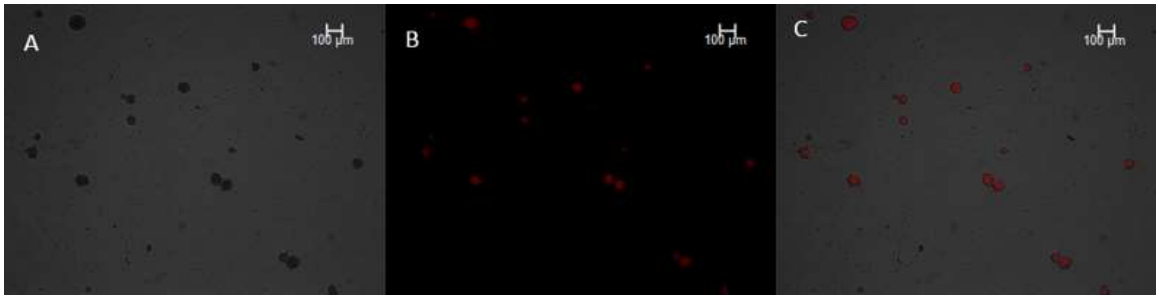

Figure 2.3 Neurospheres Labeled with 10 µL/mL of Nanoprobe for One Hour. (A) Brightfield image of NPSCs, **(B)** Fluorescent image of NPSCs (excitation: 570, emission: 590), **(C)** Overlay

2.2.2 Viability

NPSCs were labeled using previously discussed methods. Following the nanoprobe labeling protocol, cells were spun down and dissociated back into single cell form for quantitative purposes. Calcein AM live stain (Biotium; Hayward, CA, USA) was used to measure viability. Cells with co-localized signal from Nile Red and calcein AM were considered viable and labeled while cells exhibiting signal from only Nile Red were not. Viable and labeled cells were normalized against unlabeled cells for quantification.

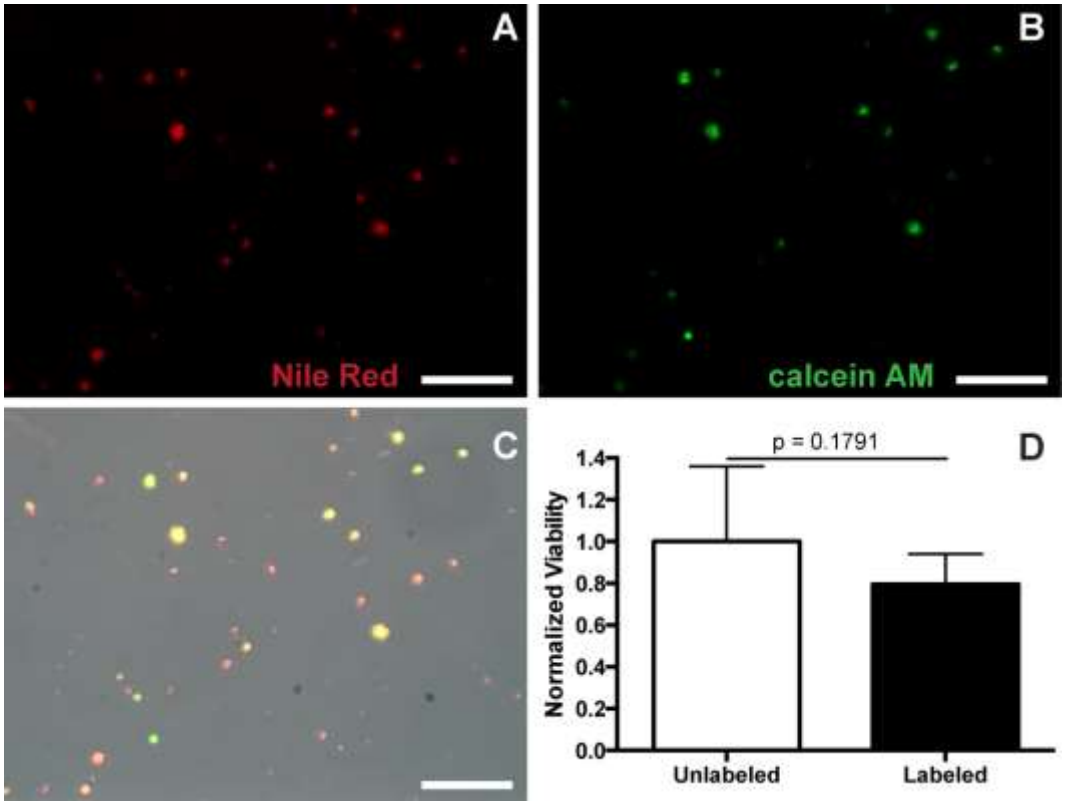

Figure 2.4 Labeled NPSC viability. Effective labeling was characterized by Nile Red **(A)** and shown viable by calcein AM **(B).** Co-localized signal **(C)** was used to determined % viability normalized to labeled cells **(D).**

Successful labeling of NPSCs was displayed at 75% viability with respect to unlabeled cells. While cells were shown to be both labeled and viable, increased viability is desirable as reported with similar stem cell labeling [18, 42]. Further studies were done to assess labeling effects on stem cell proliferation and migration.

In comparison to other labeling viability results, cell survival seems relatively low for these labeled cells. One potential study which could shed light on ways to increase viability is trypan blue exclusion or an MTT assay as shown by other studies [21, 43]. However, the MTT assay becomes difficult with the cells maintained in suspension. This study would require additional factors forcing the cells to adhere to plate surfaces for long

periods of time and eventually result in differentiation. The trypan blue exclusion stains dead cells by passing through the cell membrane. Utilizing this method may provide different results which appear more comparable with similar literature [21].

It's also important to consider the balance between labeling payload and incubation time with respect to viability. There exists an interesting balance between cell survival and amount of nanoemulsion contained within the cell. Ideally, the more emulsion the better for increased visualization during imaging. However, this increase can also be associated with negative effects on cell dynamics.

2.2.3 Migration

Following labeling, NPSC neurospheres were plated on poly-l-lysine and laminin coated surfaces. Neural progenitors have been shown to migrate on laminin surfaces and adhere, absent of migration on poly-l-lysine surfaces [44]. Neurospheres were plated in coated 24-well plates at a density of 25 neurospheres per cm^2 in growth factor-free media. 4 different well groupings were established each with n = 6: labeled cells on laminin, unlabeled cells on laminin, labeled cells on poly-l-lysine, unlabeled cells on poly-l-lysine. These groupings allowed for comparison between labeled and unlabeled cell processes. Diametrical measurements of neurosphere migration allowed for a quantitative comparison between labeled and unlabeled cells.

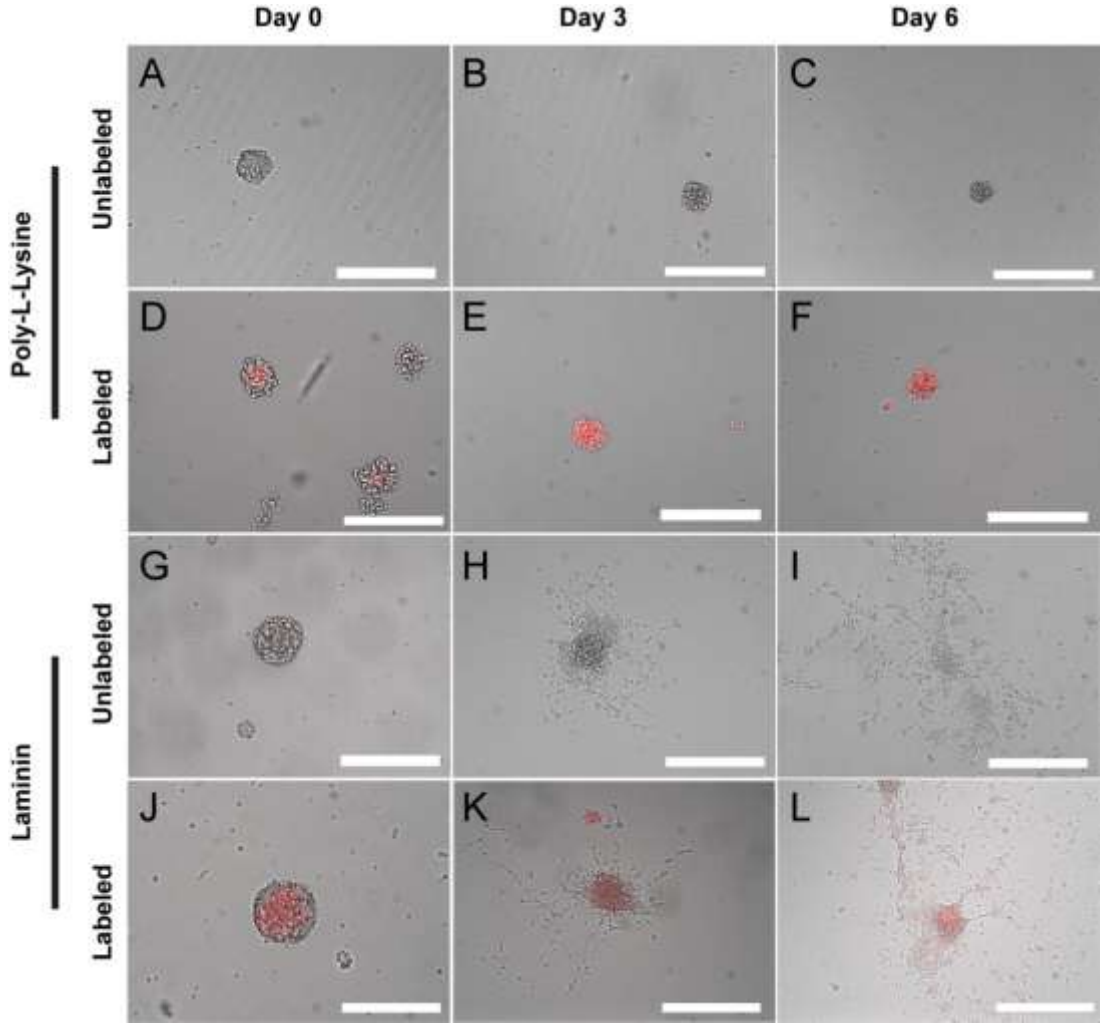

Figure 2.5 NPSC Radial Migration Out to Day 6 on Poly-l-lysine and Laminin. Both unlabeled **(A-C)** and labeled **(D-F)** NPSCs showed minimal migration on poly-l-lysine. However, significant radial migration was seen for both unlabeled **(G-I)** and labeled cells on laminin **(J-L).** Scale bar represents 150 microns.

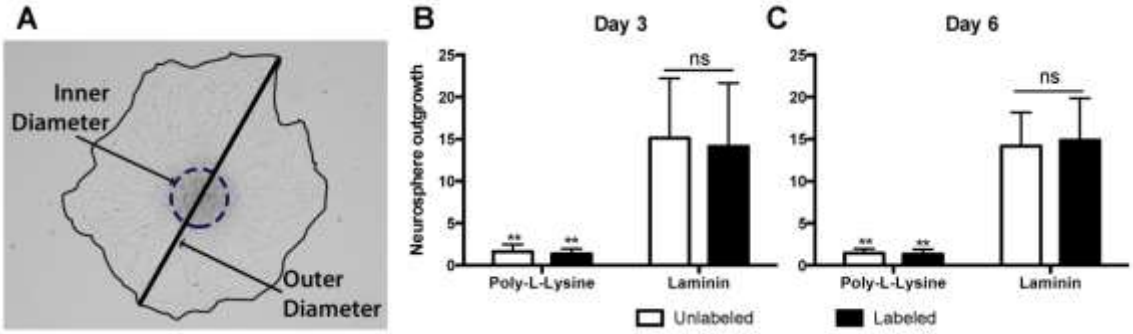

Figure 2.6 Quantification of NPSC Radial Migration. Diametrical measurements allowed for assessment on days 3 and 6 normalized to baseline measurements taken on

day 0 **(A)**. Radial migration increased on laminin for labeled and unlabeled cells and remained constant on poly-l-lysine at days 3 **(B)** and 6 **(C).** No significant differences were observed between radial migration of unlabeled and labeled NPSCs on laminin at 3 **(B)** and 6 **(C)** days. **p<0.01 compared to poly-L-lysine controls.

Comparison of unlabeled and labeled NPSCs is promising as the labeled cells behave as expected. Labeled cells migrate on laminin with no significant difference compared to unlabeled cells. Similarly, cells on poly-l-lysine withhold from migration for both labeled and unlabeled. It is encouraging to see the labeling process does not have significant effects on neural progenitor's ability to migrate.

NPSC migration is a vital step with respect to integration following transplantation. The fate of these cells appear to be more indicative of their surrounding environment rather than intrinsic properties, thus progenitor cell migration/differentiation into specific cell types for a targeted region is the foundation for potential therapies [45]. With this in mind, visualization of labeled NPSCs migration gives hope to tracking these dynamics *in vivo* and comprehending the underlying causes of integration.

2.2.4 Proliferation

The Quant-iT PicoGreen dsDNA assay kit (Life Technologies; Carlsbad, CA) was used to assess proliferation of NPSCs on poly-l-lysine at 6 days. Labeled and unlabeled neurospheres were plated on poly-l-lysine in 24-well plates (n=6) at a density of 25 neuospheres/cm^2. After 6 days, wells were scratched and lysed for 72 hours in humid conditions with Proteinase K buffer. Cells were transferred to a 96-well plate for compatibility with a fluorescence-based microplate reader. Double strand DNA quantification was performed using the assay kit. The quantitation reagent was added to the samples and a cell count was performed following plate reading.

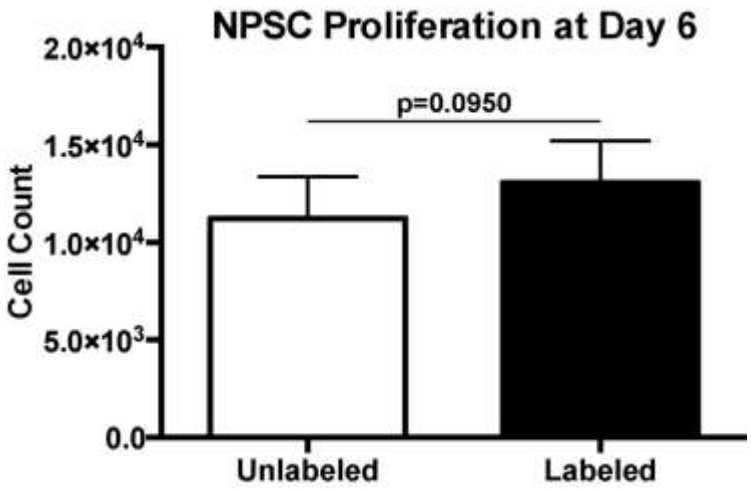

Figure 2.7 Cell count Determined after NSPC Proliferation on Poly-l-lysine for 6 Days. Labeled and unlabeled cells are not significantly different and cell counts were normalized to values on day 0.

It is promising to see labeled cells proliferating at rates similar to unlabeled cells. One important factor to consider regarding proliferation is the decreasing concentration of emulsion with proliferating cell lines. There is a finite amount of emulsion loaded within the initial labeled cells. Signal detection will become more difficult with continuing cell division, and must be acknowledged when considering long-term studies.

2.3 Cancer cell and tumor spheroid labeling

Human prostate carcinoma epithelial cell line, 22Rv1 (ATCC; Manassas, Virginia), was used for cancer cell labeling studies. Mouse embryonic fibroblast cell line, NIH/3T3 (ATCC) was used in conjunction with 22Rv1 cells for tumor spheroid formation.

Initial cancer cell studies were performed via direct labeling. As previously stated, cancer metastasis and tumor spheroid research could prove valuable areas for applicable

cell labeling. Labeling protocol for the cancer cells has remained consistent with the NPSC cells, however, recent research has shown the cells increased ability to handle longer incubation time.

22Rv1 cells were plated on T75 cell culture flasks (Fisher Scientific; Hampton, New Hampshire) and cultured using Rosewell Park Memorial Insititue (RPMI) media (ATCC). For labelling, nanoparticles were incubated with 22Rv1 cells once the cells reached 80-95% confluency at a 10 µL/mL concentration for 1-3 hours. After the incubation period, the media/nanoparticle mix was removed and the cells were washed with 3 mL of Dulbecco`s Phosphate Buffered Saline (Thermo Scientific; Waltham, Massachusetts) for 2-3 minutes. DPBS was removed and cells were trypsinized using 5 mL of Trypsin 0.25% (1X) solution (Thermo Scientific). At this point, the cells lost adherence to the flask surface, were removed, spun down, re-suspended and ready for experimental use. Labeled cells were used to make imaging phantom (discussed more in depth in Chapter 3).

Multicellular tumor spheroid formation methods are well established [31, 46]. In a 100mL Pyrex media bottle, a 1% agarose (Sigma-Aldrich; St. Louis, Missouri) gel solution was prepared using non-supplemented Dublecco's Modified Eagle's Medium (DMEM). This mixture was autoclaved, and 50µL of solution was placed in each well of a 96-well plate before solidifying. While pipetting, care was taken to ensure no bubble formation in the agarose gel. The 96-well plate was covered from light and allowed to cool for 1.5 hours.

NIH/3T3 and 22Rv1 cells were cultured alongside agarose plating. Cells were only utilized once (at minimum) 80% confluent at the time of the study. Cells were washed with DPBS, trypsinized, and re-suspended for use. The two cell lines were mixed in a 1:1 ratio

in an equal amount of DMEM and RPMI to a cell concentration of 600,000 cells/mL (final seeding density 120,000 cells/well). 200 µL aliquots were pipetted into each agarose-coated well and incubated. RPMI/DMEM mixture was added every 24-48 hours depending on nutrient uptake. Spheroids were ready for experimental use after 72 hours.

Two different methods were used to label the tumor spheroids with nanoparticle.

- Following spheroid formation, nanoemulsion was added to the DMEM/RPMI mixture at a concentration of 10 µL/mL and placed in the spheroid-containing wells. After an hour of incubation, the nanoemulsion/media solution was removed from the well. Spheroids were washed three times with PBS and placed in new wells containing nanoemulsion free media.
- NIH3T3 and 22Rv1 cells were labeled in T75 cell culture flasks as previously mentioned. After labeling, cells were trypsinzed, washed, and re-suspended to be seeded in hopes of tumor spheroid formation. 200 µL aliquots of the labeled NIH3T3 and 22Rv1 cells were added to the agarose coated wells in fresh, nanoemulsion free media.

Both labeling methodologies were examined by fluorescence microscopy.

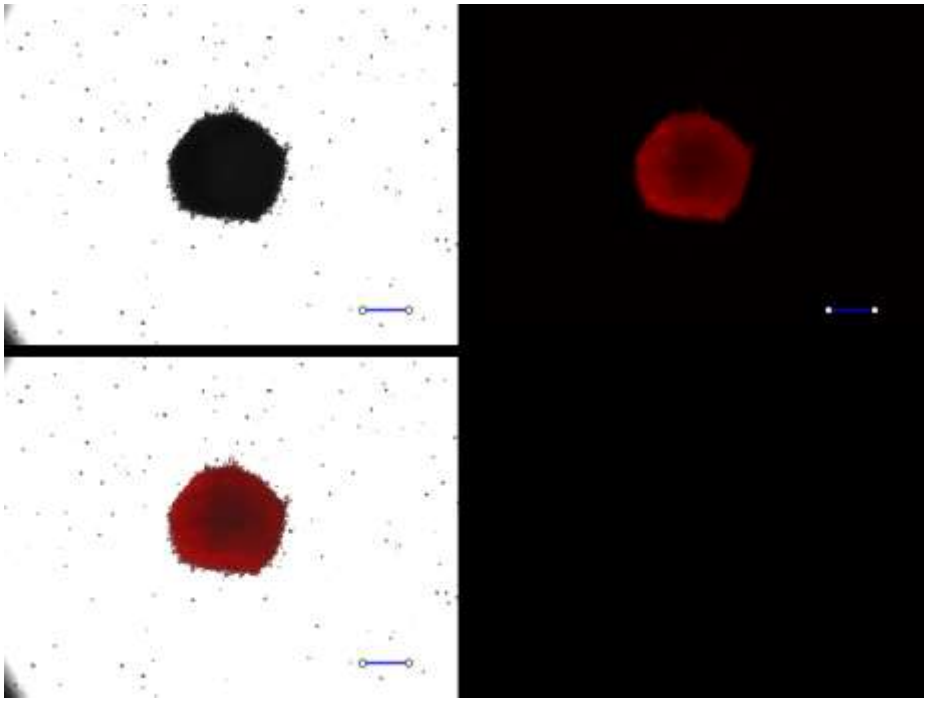

Figure 2.8 Tumor Spheroids Labeled with Nanoemulsion after Structural Formation. (A) Bright Field image **(B)** Fluorescence image **(C)** Overlay. Scale bar is 200 microns.

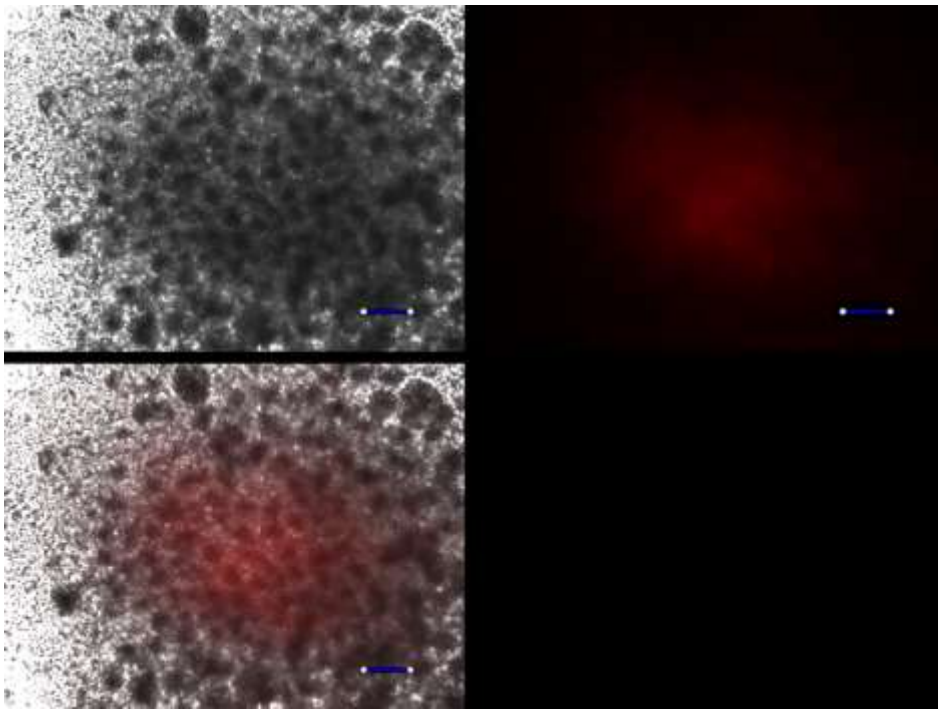

Figure 2.9 Labeled NIH/3T3 and 22Rv1 Cells Attempting to Form Tumor Spheroid at 72 Hours Post-labeling. (A) Bright Field image **(B)** Fluorescence image **(C)** Overlay Scale bar is 200 microns.

Figure 2.9 and 2.10 would lead to the conclusion of labeling after spheroid formation as the better method. However, these images do not tell the full story. Labeling after spheroid formation likely does not provide uniform labeling throughout the structure. For purposes of determining hypoxic regions within an *in vivo* tumor model, the nanoprobe would need to evenly label the spheroid to give accurate oximetry information. In this case, cells on the external portion of the spheroid are likely receiving more nanoemulsion than those on the interior.

Unfortunately, while the cells labeled pre-spheroid formation aggregated in the center of the well, complete spheroid structure was not achieved. This methodology is preferential. Labeling only the 22Rv1 cancer cells and leaving the NIH/3T3 fibroblasts unlabeled is one potential future study capable of achieving more uniform labeling. Tumor spheroid research is being revisited, and the added ability of oximetry could fuel more efficient evaluation of potential cancer agents.

CHAPTER 3

SILOXANE SELECTIVE MAGNETIC RESONANCE IMAGING

3.1 Calibration at 7T

All imaging work took place on the Pre-clinical Bruker (Billerica, MA, USA) 7T magnet at Barrow Neurological Institute/Arizona State University facilities within St. Joseph's Hospital (Phoenix, AZ). As previous experiments utilizing proton imaging of siloxane to map tissue oxygenation level (PISTOL) were done on a 4.7T magnet, calibration was required with the change in field strength.

Calibration experiments were done to characterize the effects of pO_2 on spin lattice (longitudinal) relaxation rate, R_1. The interaction between oxygen and HMDSO, an oxygen reporter molecule, is advantageous in quantitative MR oximetry. The oxygen molecule is paramagnetic and tends to cause nuclear spins to relax at faster rates – therefore increasing the R_1 and R_2 of the siloxane. A requirement for siloxanes used in quantitative MR oximetry is high oxygen solubility. In this way, increased presence of oxygen will cause an increase in relaxation rate.

Based on previously established ways to model tissue oxygenation [47, 48], we can consider oxygen reporter molecules with high concentrations of oxygen in their vicinity and conversely, oxygen reporter molecules with low concentrations of oxygen in their vicinity. The high solubility of oxygen in the reporter molecule allows us to look at the relaxation rate for each reporter molecule (high O_2 conc. and low O_2 conc.) as a molar weighted average. The net relaxation rate can be evaluated considering x as the molar fraction of oxygen by the following equation

$$R_1 = (1 - x)R_{1d} + x(R_{1d} + R_{1p}) = R_{1d} + x(R_{1p}) \quad [7]$$

Where R_{1d} is the relaxation rate when no oxygen is present (anoxic conditions), R_{1p} is the paramagnetic component of the relation rate due to oxygen uptake, and R_1 is the relaxation rate ($1/T_1$). The partial pressure of a gas is directly related to the mole fraction based on the following relationship.

$$P_1 = x(P_{tot}) \quad [8]$$

Where P_1 is the partial pressure of a gas, x is the mole fraction, and P_{tot} is the total pressure of the gas. Similarly, the partial pressure of oxygen (pO_2) is related to the mole fraction by an agent dependent constant (k) that determines the solubility of oxygen in the agent.

$$pO_2 = k(x) \quad [9]$$

Therefore, the relationship between longitudinal relaxation rate and pO_2 becomes

$$R_1 = A' + B'*(pO_2) \quad [10]$$

where $A' = R_{1d}$ and $B' = R_{1p}/k$

Longitudinal relaxation rate is a function of temperature, and thus the constants A' and B' have an assumed linear dependence on temperature. This relationship can be defined as

$$A' = A + C*(T) \quad [11]$$

$$B' = B + D*(T) \quad [12]$$

The goal of defining these constants for HMDSO and PDMS at higher field strength was in mind when running initial experiments.

Neat HMDSO (Sigma-Aldrich) was placed in four John Young NMR tubes at 200 µL volumes. Using a sealed environment free from ambient air, samples were bubbled with gas at different concentrations of oxygen with a Hypoxydial™ Gas Blender (Starr Life Sciences; Oakmont, Pennsylvania, USA). These concentrations included 0% (anoxic), 5%,

10% and 21% oxygen. Samples were sealed so that proper oxygen concentrations remained unchanged upon interaction with the environment.

The four J. Young NMR (Wilmad-Labglass; Vineland, NJ, USA) tubes were placed together and put into the bore of the magnet on top of a heated water bath extension provided by Bruker. Temperature was measured with an MR compatible temperature probe to confirm water bath measurements. Using the PISTOL sequence developed by Dr. Vikram Kodibagkar and implemented on the Bruker system by Rohini Shankar, frequency-selective signal detection of the HMDSO was achieved. T1 mapping was employed to measure the longitudinal relaxation rate ($R_1 = 1/T_1$). The experiment was repeated at for a total of four different temperature points: room temperature (23.5ºC), 27ºC, 32ºC, and *in vivo* temperature (37ºC).

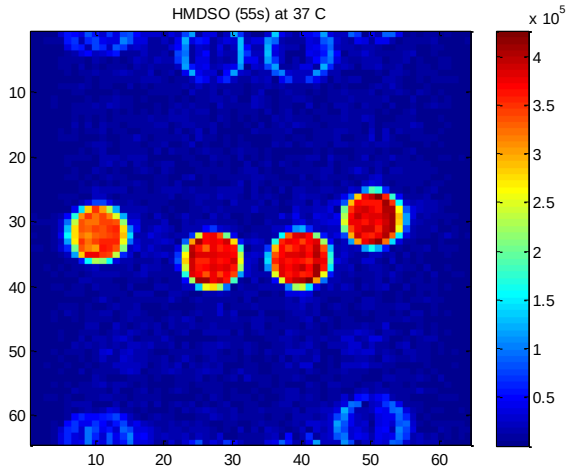

Figure 3.1 Neat HMDSO Signal Acquisition via Proton Imaging of Siloxanes to map Tissue Oxygenation Level. Repetition time (TR = 55s) at 37ºC displays signal from all four John Young NMR tubes.

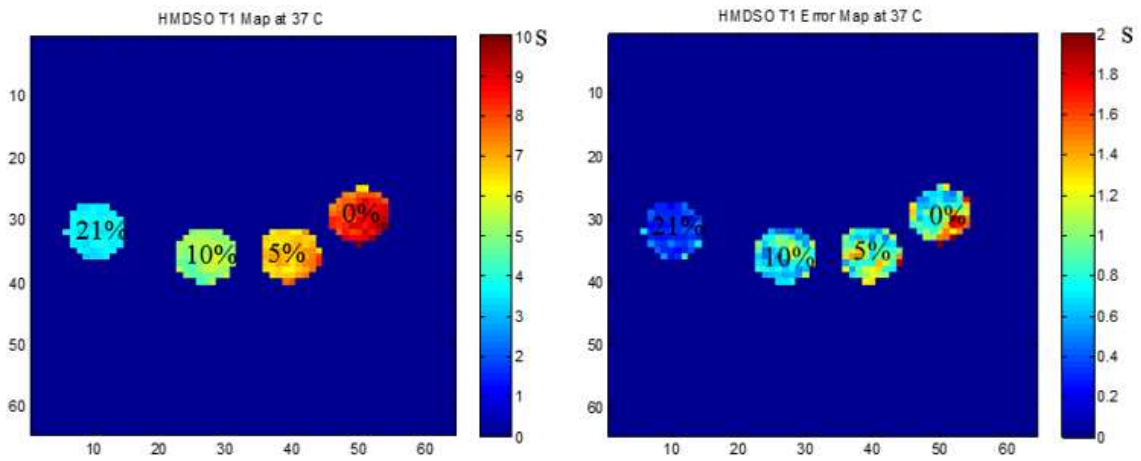

Figure 3.2 T_1 Mapping of Neat HMDSO-containing John Young NMR Tubes in 21%, 10%, 5%, and 0% Oxygen Concentrations. A decreased T_1 relaxation time is displayed with increasing pO_2.

R_1 values at varying temperatures were plotted as a function of pO_2 (in torr). In this way, determination of the constant, A', occurs at the intercept of the linear fit because when pO_2 is equal to zero torr, $R_1 = A'$. Similarly, the constant B' can be determined by the slope of the linear fit. When pO_2 is not equal to zero, the longitudinal relaxation rate is governed by the paramagnetic component of relaxation rate due to oxygen uptake based on amount of solubilized oxygen. The constants C and D can be determined by plotting A' and B' values with respect to temperature. Based on the following equation, a more accurate and reliable calculation of pO_2 can be achieved.

$$R_1 = A' + B'*(pO_2) + C*T + D*T*(pO_2) \quad [13]$$

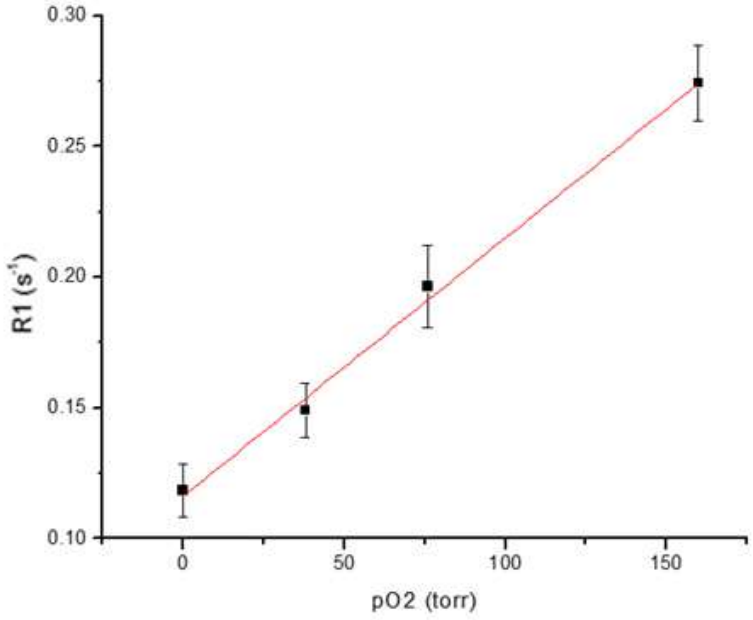

Figure 3.3 Neat HMDSO R1 Values of 0%, 5%, 10%, and 21% Oxygen Concentrations at 37ºC. Calibration constant A' = 0.11631 ± 0.002 based on linear fit, calibration constant B' = 0.000988 ± 0.00003, R^2 =0.99751

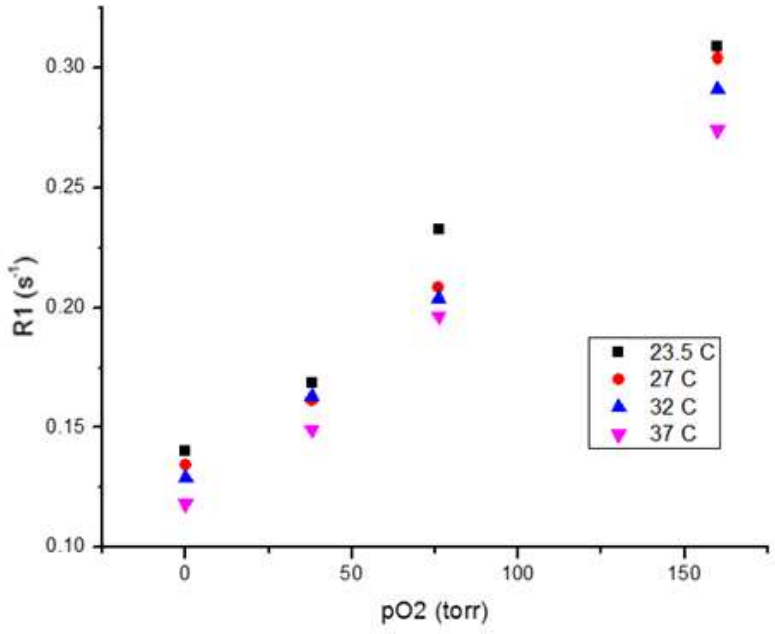

Figure 3.4 Neat HMDSO R1 Values at Varying Temperatures. Values decrease slightly with increasing temperature at temperatures 23.5ºC, 27ºC, 32ºC, and 37ºC.

After determining the A' and B' values at each temperature point, these values can be plotted as function of temperature. C and D constants can be determined via the relationships in equation 11 and 12.

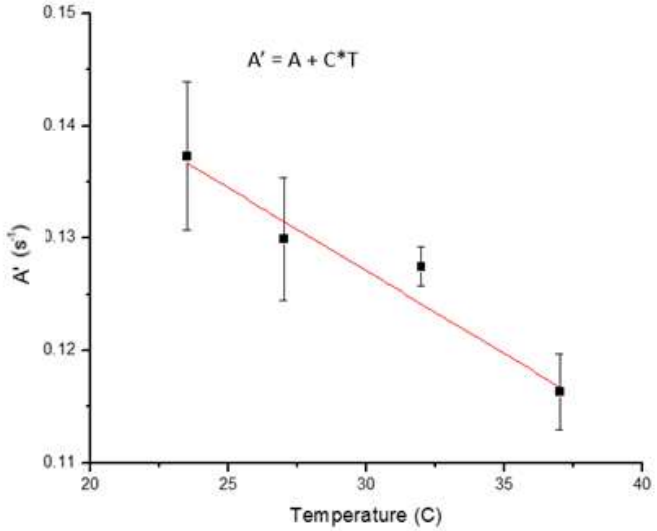

Figure 3.5 Neat HMDSO Temperature Dependence of Constant A' at 7T. Linear fitting resulted in calibration constants A = 0.1714 ± 0.00587 and C = -0.00148 ± 0.002, R^2 =0.944

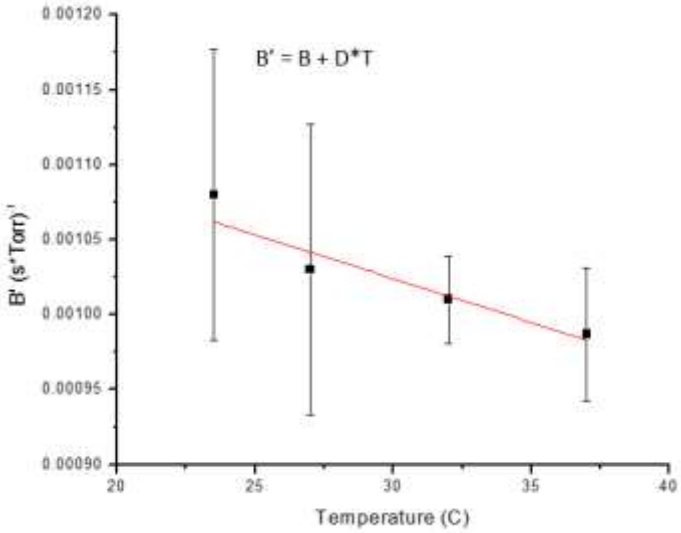

Figure 3.6 Neat HMDSO Temperature Dependence of Constant B' at 7T. Linear fitting resulted in calibration constants B = 0.0012 ± 0.000004 and D = $-5x10^{-6}$ ± 0.000001, R^2=0.8865

Determination of these constants allows for a complete picture of relaxation rate with respect to pO_2. Similar experiments were done using PDMS at 37ºC, however, a leak in one of the John Young NMR tubes caused PDMS at 0% oxygen to interact with ambient air and behave more like PDMS at an oxygen concetration close to atmospheric levels. Therefor, this value is ignored.

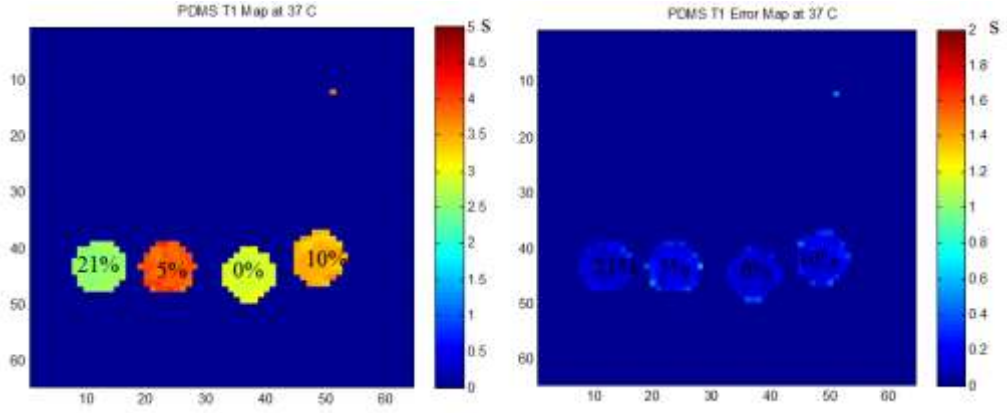

Figure 3.7 T_1 Mapping of Neat PDMS-containing John Young NMR Tubes at 21%, 10%, 5%, and 0% Oxygen Concentrations. A leak in the "0% concentration" tube effected data and was ignored when plotting R_1 with respect to pO_2.

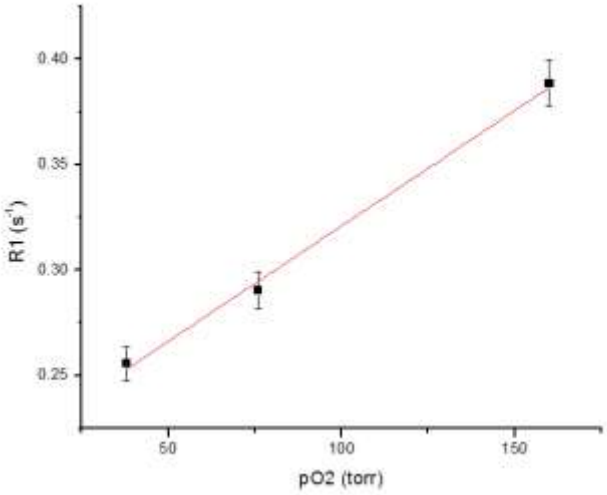

Figure 3.8 Neat PDMS R1 Values at 5%, 10%, and 21% Oxygen Concentrations (37ºC). Calibration constant A' = 0.21156 ± 0.00608 based on linear fit, calibration constant B' = 0.00109 ± 0.00007, R^2 =0.9926

For PDMS-based nanoemulsions, similar experiments were run at 23ºC for calculations involving *in vitro* samples and 33.5ºC (discussed later) for *in vivo* calculations.

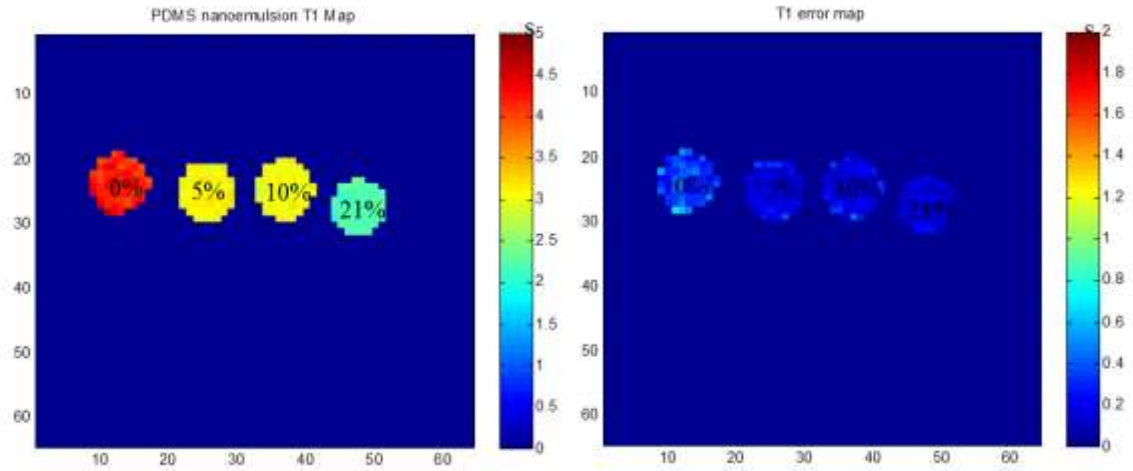

Figure 3.9 T_1 Mapping of PDMS Nanoemulsions in John Young NMR tubes at 21%, 10%, 5%, and 0% Oxygen Concentrations. A leak in the 5% oxygen concentration tube skewed data and was ignored for constant determination.

After the R_1 relaxation rates were plotted against pO_2, it was determined the 5% oxygen sample was incorrectly processed. The average T_1 value within the 5% and 10% samples were 3.43 and 3.28 seconds respectively at 33.5ºC. While these numbers continue the expected trend of decreased R_1 value with decreased pO_2, linear fitting showed the 5% sample to deviate from the expected trend based on PDMS and HMDSO data. For this reason, the 5% sample was excluded from linear fitting to attain constants.

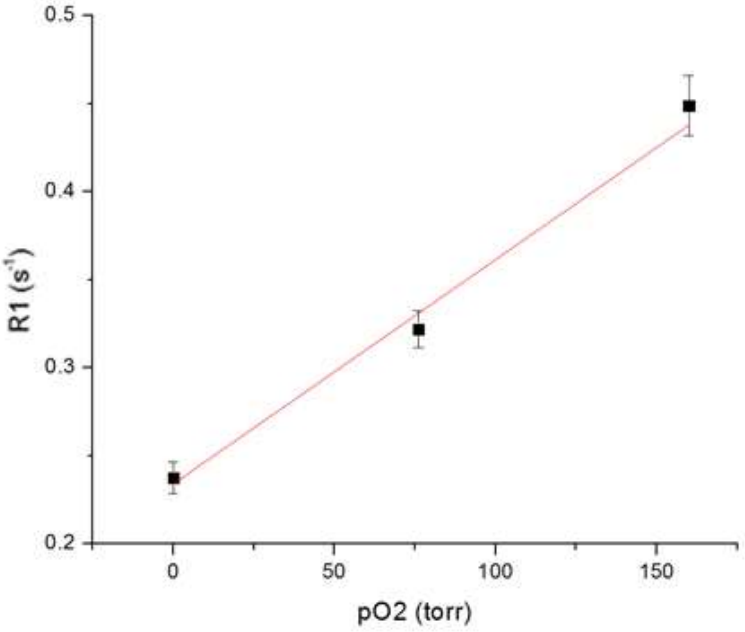

Figure 3.10 PDMS Nanoemulsion R1 values at 0%, 10%, and 21% Oxygen Concentrations (23ºC). Calibration constant A' = 0.234 ± 0.00967 based on linear fit, calibration constant B' = 0.00127 ± 0.00012, R^2 =0.97988

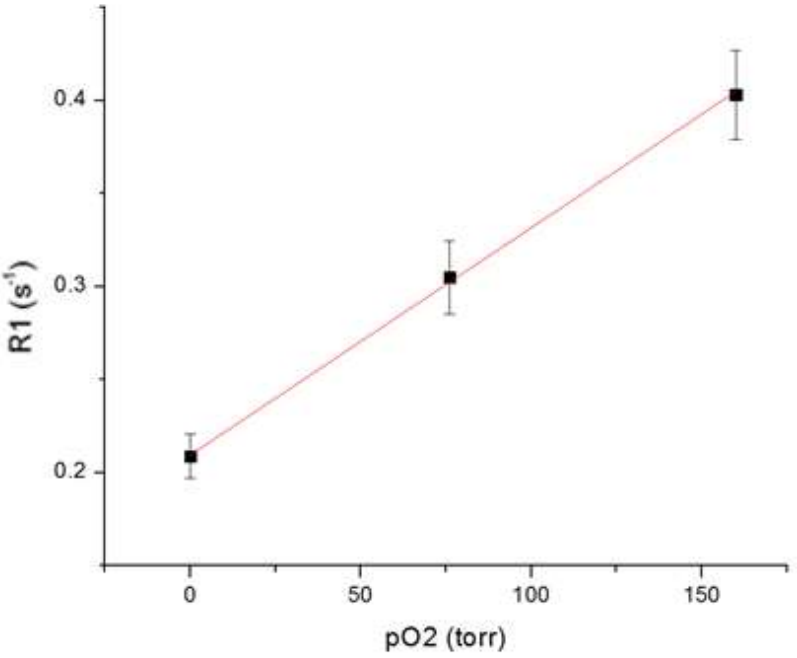

Figure 3.11 PDMS Nanoemulsion R1 Values at 0%, 10%, and 21% Oxygen Concentrations (33.5ºC). Calibration constant A' = 0.20948 ± 0.00176 based on linear fit, calibration constant B' = 0.00122 ± 0.000024, R^2 =0.992

While calibration work will not inherently change the relxation rates or MR-based parameters, proper constants are important for accurate oximetry. PDMS nanoemulsions were calibrated at room temperature (23ºC) and a temperature near *in vivo* (33.5ºC). Unfortunately, 33.5ºC was the highest temperature measured when maxing out the water bath provided by Bruker. The water bath has the capability to heat to 37°C, but was malfunctioning during the experiment, and could not heat to the appropriate level. While it is not precisely *in vivo* temperature, it is a close approximation. Additionally, the values attained while measuring values of PDMS at 37°C appear to be comparable to emulsion values at 33.5°C. One way to confirm these values is to acquire the C and D constants as shown in figures 3.5 and 3.6. These constants allow for a more complete look at relaxation rate.

It is encouraging to see T_1 relaxation time decrease with increasing oxygen concentration. It has been shown that T_1 increases with increased temperature and thus, a decrease in R_1 is displayed. These relationships can be seen in calibration of HMDSO, PDMS, and PDMS-based nanoemulsions.

In comparison to previous values acquired at the University of Texas-Southwestern by Dr. Kodibagkar and his students (specifically Ujjawal Rastogi), the constants acquired using the 7T magnet are comparable. In theory, T_1 relaxation times should increase with higher field strength. This is due to the increased net bulk magnetization. Higher energy spin states outnumber lower energy spins to a greater extent at higher fields. These changes in T_1 relaxation times require calibration at new fields and with new siloxanes.

3.2 MR imaging of NPSCs

As previously discussed in Chapter 2, NPSCs have been labeled and imaged using fluorescence microscopy. NPSCs are imaged in 2.0 mL microcentrifuge tubes (Eppendorf; Hamburg, Germany) surrounded by a 2% agarose gel (Sigma-Aldrich). Agarose gels were fabricated by placing 200mg of agar in 10 mL of deionized water within a 20 mL glass vial. This mixture was heated above 90ºC while stirred.

Cells were labeled as per previous studies' protocol, spun down in Falcon™ 15mL Conical Tubes (Fisher Scientific), and re-suspended in 1.0 mL fresh, nanoemulsion-free media. A 750µL base layer of agar was placed in the 2.0 mL microcentrifuge tube and placed on ice for cooling. Once solidified, 1.0 mL of re-suspended, labeled NPSCs were pipetted on top of the base layer. This sample was centrifuged for a second time (1000 rpm) for 5 minutes, with a cell pellet forming on top of the initial agarose layer. A second 1.0 mL layer of liquid agarose was pipetted gently on top of the cell pellet so as to minimize bubble formation.

It is important to surround the cell pellet with agarose and keep the pellet away from tube surfaces because of the susceptibility artifact. This artifact is caused by interaction between surfaces which tend to distort the applied magnetic field via local inhomogeneities [49]. Echo-planar imaging (EPI), a technique utilized by PISTOL, is especially prone to this artifact due to the inhomogeneities near interfaces [50].

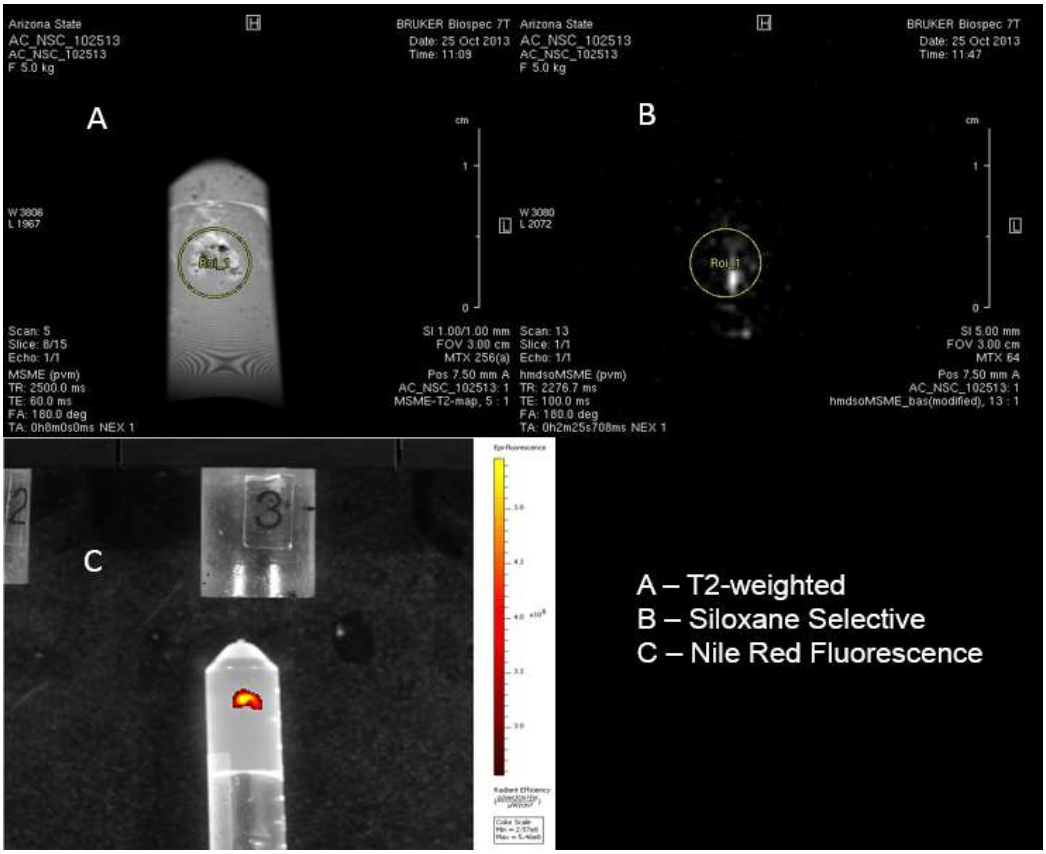

Figure 3.12 Dual-modality Imaging of Labeled NPSC Pellet. T2-weighted scout scan of labeled stem cell pellet submerged in agarose gel (A), Siloxane-selective image (B), Fluorescence image: excitation – 500 nm, emission – 560 nm (C)

Figure 3.12 shows the dual-modality nature of the labeled NPSCs. 400,000 NPCs were labeled and imaged using a siloxane-selective multi-slice, multi-echo image. Fluorescence imaging was done using an Invitrogen bioluminescence/fluorescence imaging device (Life Technologies). However, the MR image does not give the precise signal detection desired, and following work tried to combat sensitivity issues involving detection. A promising cell pellet imaging phantom was produced using 400,000 cells and shifted signal (susceptibility artifact) was detected. To ensure the signal was in fact from the nanoprobe-labeled cells, chemical shift imaging was employed.

Chemical shift imaging maps the spatial distribution of nuclei associated with a specific chemical shift (ie. Hydrogen groups associated with water, lipids, or siloxanes) [51]. In this way, we can look at the NMR spectra within a specific location and determine if siloxane signal is present.

A metabolite map was created using computing program, Matlab (Mathworks, Natick, Massachusetts, USA), and overlaid with an anatomical T_2-weighted image to display location of siloxane. As displayed in Chapter 1.4, PDMS is located 4.2 – 5.2 ppm from water on an chemical shift spectra. When centering water's resonance at 0 Hz, PDMS is located roughly 1425 Hz away from water.

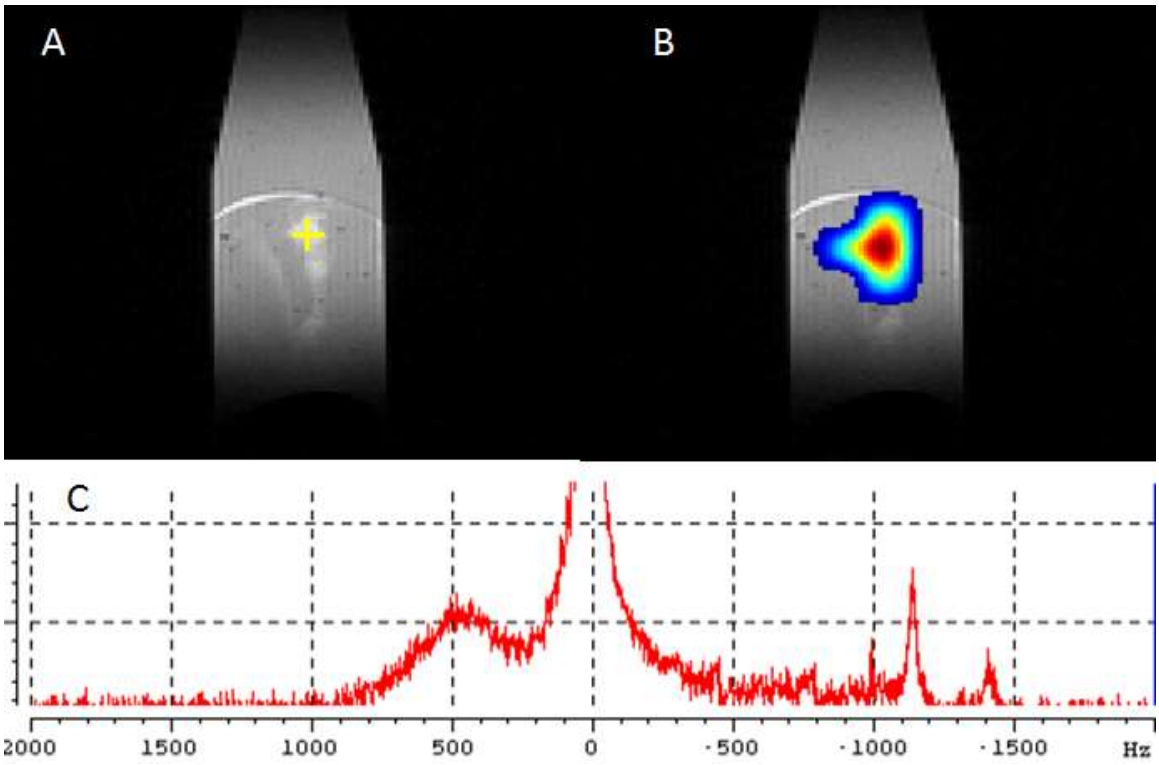

Figure 3.13 Chemical Shift Imaging and Metabolite Map of Labeled NPSC Pellet. CSI shows signal from nanoprobe-labeled NPSCs (signal near 1425 Hz away from water at 0 Hz). **(A)** T_2-weighted anatomical image with marker for NMR spectra viewing **(B)** Metabolite map overlay **(C)** Chemical shift imaging NMR spectra

These results showed the presence of siloxane signal in NPSCs. The yellow marker shows the voxel at which the CSI spectra was created. After imaging of siloxane labeled cells was shown feasible, *in vivo* experiments took place tranplanting labeled NPSCs into the mouse brain.

Animal experiments were done in accordance with approval by the Institutional Animal Care and Use Committee at Arizona State University. C57BL/6 mice were anastethized and placed on a stereotactic device. Incisions were made allowing for Hamilton needle (Hamilton; Reno, NV, USA) injections in correlation with a nanoinjector. 5 µL of labeled NPSCs in working media were injected and the incision area was sutured shut. This method has yet to been validated with MR data, but experimental design is being altered to overcome sensitivity issues.

However, in the controlled cortical TBI model, MR signal has been acquired from the PDMS-based nanoprobes. Using a 2 mm diamter electromagnetic piston (Leica Microsystems; Wetzlar, Germany), an injury was inflicted on C57BL/6 mice. The piston was delpoyed at 5m/s for 2 ms at a depth of 1.5 mm into the brain. Animals were injured 1 week prior to injection of 10 µL of nanprobe and subsequent imaging.

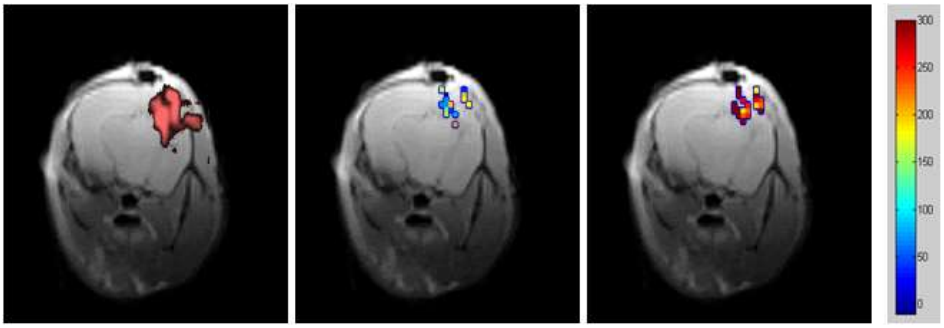

Figure 3.14 Siloxane Selective MR Data Overlaid on Grayscale T_2 Anatomical Images. Displayed are siloxane signal **(A)**, air breathing **(B)** and oxygen breathing **(C)** with mean pO_2 values of 54 torr and 154 torr respectively.

Air and oxygen breathing help to verify the presence of siloxane, an oxygen reporter molucule, as the increased presence of oxygen should result in a decreased T_1 relaxation time. The injection of PDMS-based nanoprobe helps to prove the concept of detection and oximetry for NPSC transplantation applications. The implementation in the traumatic brain injury model is ideal for long-term goals. The overall goal is theranostics, and neural stem cell transplantation has shown promising effects post-TBI.

Most recently, a similar imaging phantom was fabricated using slightly different labeling parameters. Due to sensitivity issues, an aim to increase labeling payload was targeted. Using 950,000 cells and a 3 hour incubation time, NPSCs were labeled. Instead of immersing the labeled pellet in two layers of agar, the NPSCs were washed in DPBS and re-suspended using 100 µL of agarose. This experiment best replicates the injection of a NPSC loaded gel, and brings the study closer to overcoming the sensitivity obstacles.

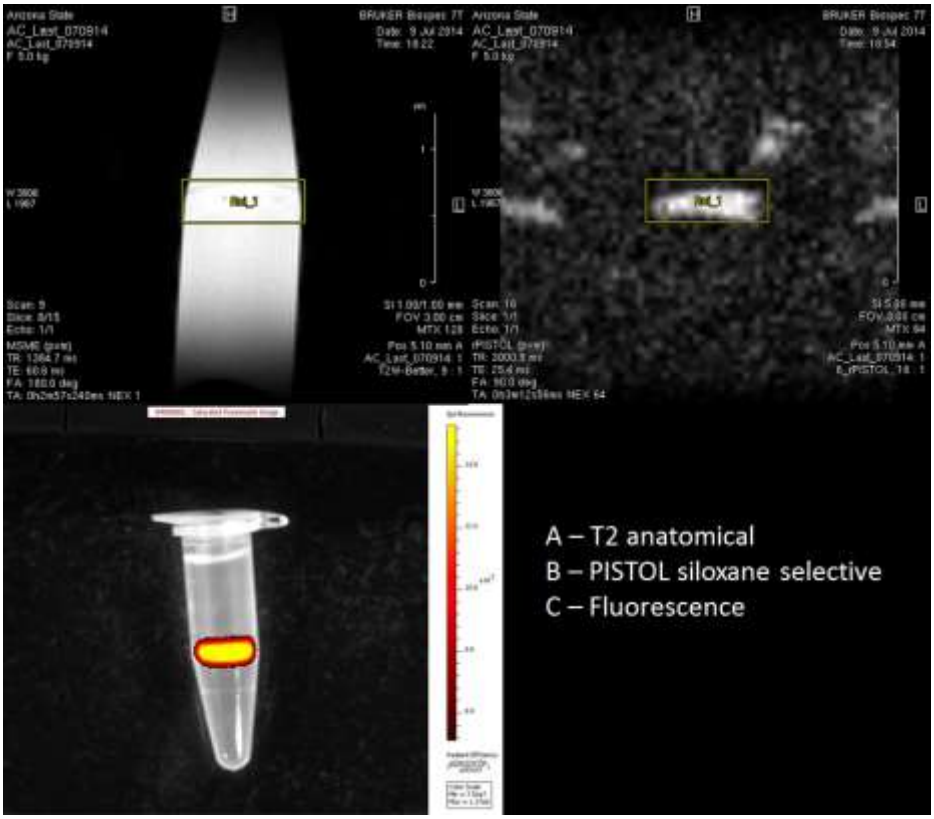

Figure 3.15 Dual-modality Imaging of Labeled NPSCs Suspended in Agarose. T2-weighted scout scan of labeled NSPCs in 100 µL agarose gel **(A),** PISTOL image **(B)**, Fluorescence image: excitation – 500 nm, emission – 560 nm **(C)**

Increased incubation time and cell count provides an increased opportunity for detection and may hold the key to overcoming sensitivity issues. Future studies will acquire images using the PISTOL sequence at different repetition times in order to create a complete T_1 map.

3.3 Cancer Cell MR imaging

Cancer cells were labeled using the same protocols discussed in Chapter 2. For the imaging phantom shown below (Figure 3.16), 4,000,000 22Rv1 cells were labeled, re-suspended in agarose gel, and placed in 1 mm diameter Wilmad NMR capillary tubes

(Sigma-Aldrich). Similar samples were made in capillary tubes using 1,000,000 labeled cells and pure agarose absent of cells. This method was utilized in an attempt to quantify signal intensity with respect to cell count.

For tumor spheroid imaging, spheroids were labeled after structural formation as described in Chapter 2. Spheroids were immersed in agarose gel within 2.0 mL microcentrifuge tubes to minimize susceptibility.

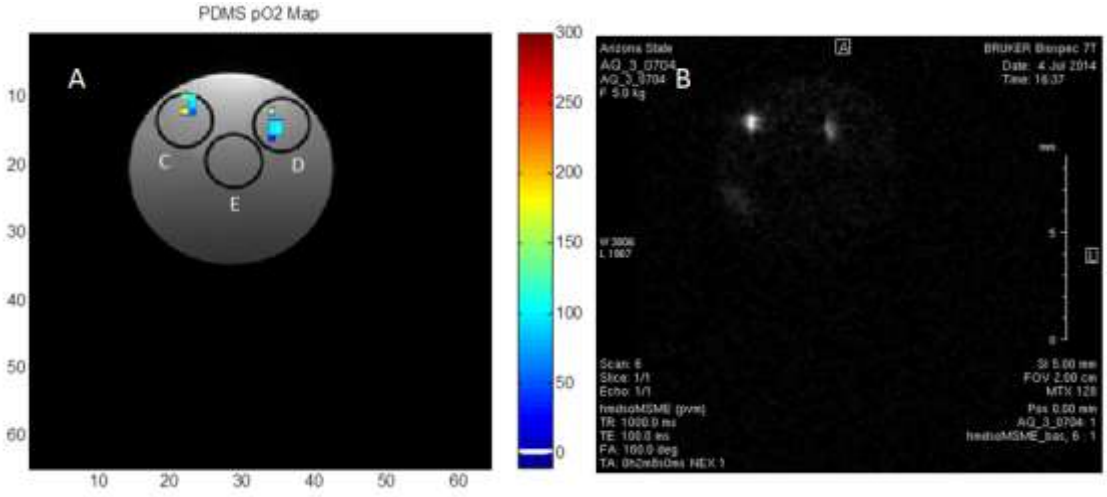

Figure 3.16 Siloxane Selective Imaging of Cancer Cells at Different Concentrations. PISTOL overlay on T2 anatomical image **(A)** with 4 X 10^6 cells in **C**, 1 X 10^6 cells **D**, and zero cells in **E** with mean. A mean pO_2 value of 95 torr was determined for all cells. A multi-slice, multi-echo siloxane selective sequence is shown with signal corresponding to the cell containing tubes (**B)**.

The location of the signal in the PISTOL overlay is concerning. Cells were placed throughout the capillary tube and it is expected signal would be acquired across the entire diameter of the tube. Additionally, the mean pO_2 values (at 95 torr) are less than we would expect in ambient air. Again, longer incubation times could provide for a higher payload of nanoemulsion within the cells and potentially give a signal increase.

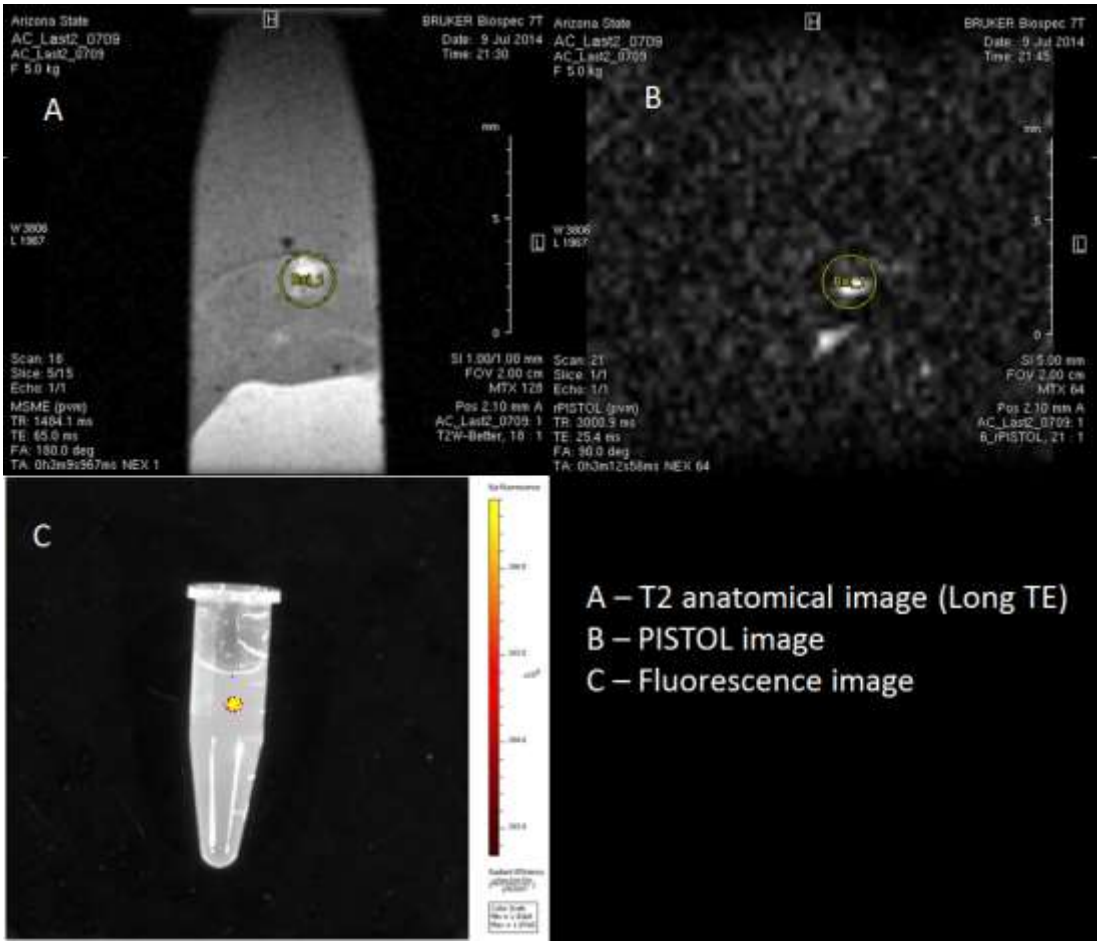

Figure 3.17 Dual Modality Imaging of Labeled Tumor Spheroid. T2-weighted scout scan of labeled tumor spheroid immersed in agarose gel **(A)**, PISTOL image **(B)**, Fluorescence image: excitation – 500 nm, emission – 560 nm **(C)**

The number of averages in the PISTOL image was 64, and future experiments will vary the repetition time using this sequence to acquire a complete T_1 map. Figure 3.17 displays the ability to view labeled spheroids *in vitro*. With continued experimentation in the spheroid fabrication process, aims include a more uniformly labeled spheroid for a complete look at modeled hypoxic regions. It is encouraging to see localized signal from where the spheroid appears to be on the T_2 anatomical image and correlating PISTOL imaging. Using a long echo time, signal from water and fat decrease while siloxane signal remains bright per its long T_2.

CHAPTER 4

DISCUSSION AND CONCLUSION

The sensitivity issues in imaging are a delicate balance, and further research needs to be conducted in order to determine the labeling "sweet spot". On one hand, increasing the incubation time, and the amount of nanoparticle loaded into either NPSCs or cancer cells will increase MR signal. However, increased labeling could result in greater effects on cell functionality and thus, disrupting the processes essential for therapy/detection post-transplantation.

From an imaging standpoint, higher field strength imaging will potentially result in more signal. A stronger magnet creates a larger discrepancy between high energy and low energy nuclear spins creating a larger bulk magnetization when a sample is exposed to an external magnetic field [52]. Additionally, signal to noise ratio increases at higher fields. Unfortunately, most clinical imaging is done at 1.5 and 3T fields at lower strength than the Bruker 7T. Nonetheless, signal detection is more than possible at the current fields, it becomes a matter of parameter optimization.

Considering a 5 µL injection into the mouse brain as per the established protocol calls for, and assuming all of that 5 µL is cell. Taking it another step further and assuming these cells were 100% labeled with nanoprobe. This assumption would leave, at best case scenario, 2 µL of siloxane for detection. While this value is entirely plausible for signal detection, actual conditions likely call for detection at near an order of magnitude less.

MRI has been shown capable of detecting single particles at the micron level [53]. Additionally MRI has proven able to detect single cells following transplantation [54].

At small resolutions, particles of sizes 0.76 μm – 1.63 μm indicated T_2 effects [53]. These experiments occurred on an 11.7T magnet, so for sake of comparison, taking the high-end particle size for a baseline detection estimation is necessary. With a particle diameter of 1.63 μm, the volume of one particle is 18.14 μm^3. Based on the relationship 1 mL is equivalent to 1 cm^3, 1 μm^3 is equivalent to $1x10^{-9}$ μL. Therefore, at 11.7T, MR effects are shown at contrast agent levels of $1.8x10^{-8}$ μL. And as noted by Shapiro et. al, detection of particles below 0.96 μm becomes difficult.

By looking at our earlier example – which considered 2 μL as the maximum amount of siloxane present within a 5 μL NPSC slurry injection -- it is fair to assume detection of nanoprobe within labeled cells is probable. However, there are some additional considerations to take into account.

Realistically, the maximum 2 μL estimation is generous and is more likely an order of magnitude less. The injection is not 100 percent cells, and these cells are not 100 percent labeled. A better estimation would be to consider the cells 10 percent labeled resulting in a maximum of 0.2 μL of siloxane injected into the brain. Again, the injected slurry is not an ideal injection and is more likely to give a maximum siloxane volume somewhere within the window of 0.1 μL – 0.2 μL. This cautious estimation still lies well within the limits of detection as displayed by Shapiro. With this in mind, identifying ways to increase siloxane detection is the next step in successful experimentation.

Iron oxide particles are considered superparamagnetic, and the term "superparamagnetism" refers to the behavior of the particle's magnetic moment with respect to eliminating magnetic interaction in the presence of the external magnetic field [55]. Therefore, contrast is enhanced via "signal loss" or a darkening on T_2 weighted

images. This occurs via the shortening of T_2 relaxation rates and can be referred to as negative contrast. The siloxane contrast agents mentioned here work in a different way. These nanoprobes rely on the frequency-selective excitation of siloxane resonance and chemical-shift suppression of other ^1H sources. This is considered a positive contrast agent due to the generation of signal on siloxane-selective sequences.

While at the core of both techniques lie interactions between magnetic moments and the external magnetic field, the siloxane contrast agents are susceptible to artifacts, and acquisition parameters must be optimized. Chemical shift edge artifacts [56, 57] can occur, but the more applicable concerns involve the susceptibility artifact and background signal elimination. These concerns can be addressed with increased attempts at boosting local field homogeneity (shimming) and suppression techniques. Fat resonance is of additional concern as the lipid bi-layer constructing most cell membranes tends to have a chemical shift near siloxane. Overcoming these issues is plausible, but they stress the emphasis on optimal conditions during acquisition.

Another consideration that will impact studies across the board is incubation time. Iron oxide studies have shown an overnight incubation with contrast agent (prior to washing) [54, 58], and an increase in iron oxide content within the cell with longer incubation times [58]. It's rather intuitive to assume a longer incubation time will result in a higher loading yield. The original incubation time of one hour was determined based on the already low viability post-labeling, and the appearance of successful labeling on fluorescence microscopy after one hour. In comparison to other labeling techniques [21, 42] the proposed incubation time tends to be on the low end. Of course, a longer incubation time is desired, but this also brings up viability and functionality questions. Previously, we

had seen migration viability concerns on the Day 6 time point, but re-testing viability, migration, and proliferation with a longer incubation time could be the key to *in vivo* signal detection.

In vitro studies have been promising, and increasing the amount of nanoprobe within the cell could be the factor that gives more promising *in vivo* data.

Additional *in vivo* data could be generated with cancer cells as injection limitations are less stringent. However, we must consider cell functionality amidst excessive loading. While tumor spheroids have been successfully labeled, forming spheroids out of pre-labeled cells has shown issues in structural formation. Further studies will address some of the setbacks in this experimentation, and should provide a valuable oximetry tool for further cancer evaluation.

Contrast agents utilized in conjunction with ^{1}H MRI have advantages in cell labeling applications. Contrast generation is a useful tool for *in vivo* tracking at the cellular level. Oximetry is beneficial for evaluating cancer metabolism and injury dynamics. A better understanding of the labeling process, and technique enhancement, will provide a valuable tool for therapy investigation and cell tracking.

REFERENCES

1. Murphy, G., et al. "Phase I clinical trial: T-cell therapy for prostate cancer using autologous dendritic cells pulsed with HLA-A0201-specific peptides from prostate-specific membrane antigen." The Prostate 29.6 (1996): 371-80

2. Kim, Jong-Hoon, et al. "Dopamine neurons derived from embryonic stem cells function in an animal model of Parkinson's disease." Nature 418.6893 (2002): 50-56.

3. Fearnley, Julian M., and Andrew J. Lees. "Ageing and Parkinson's disease: substantia nigra regional selectivity." Brain 114.5 (1991): 2283-2301.
4. Himmelreich, Uwe, and Mathias Hoehn. "Stem cell labeling for magnetic resonance imaging." Minimally Invasive Therapy & Allied Technologies 17.2 (2008): 132-142.

5. Caravan, Peter, et al. "Gadolinium (III) chelates as MRI contrast agents: structure, dynamics, and applications." Chemical reviews 99.9 (1999): 2293-2352.

6. Ruiz‐Cabello, Jesús, et al. "Fluorine (19F) MRS and MRI in biomedicine." NMR in Biomedicine 24.2 (2011): 114-129.

7. Gulaka, Praveen K., et al. "Hexamethyldisiloxane‐based nanoprobes for 1H MRI oximetry." NMR in biomedicine 24.10 (2011): 1226-1234.

8. Vuu, Kien, et al. "Gadolinium-rhodamine nanoparticles for cell labeling and tracking via magnetic resonance and optical imaging." Bioconjugate chemistry 16.4 (2005): 995-999.

9. Valable, Samuel, et al. "In vivo MRI tracking of exogenous monocytes/macrophages targeting brain tumors in a rat model of glioma." Neuroimage 40.2 (2008): 973-983.

10. Janjic, Jelena M., et al. "Self-delivering nanoemulsions for dual fluorine-19 MRI and fluorescence detection." Journal of the American Chemical Society 130.9 (2008): 2832-2841.

11. Menon, Jyothi U., et al. "Dual-modality, dual-functional nanoprobes for cellular and molecular imaging." Theranostics 2.12 (2012): 1199.

12. Centers for Disease Control and Prevention: Traumatic Brain Injury, 2014

13. Ghajar, Jamshid. "Traumatic brain injury." The Lancet 356.9233 (2000): 923-929.

14. Kay, Thomas. "Neuropsychological treatment of mild traumatic brain injury." The Journal of Head Trauma Rehabilitation 8.3 (1993): 74-85.
15. Tajiri, Naoki, et al. "Stem Cell Recruitment of Newly Formed Host Cells via a Successful Seduction? Filling the Gap between Neurogenic Niche and Injured Brain Site." PloS one 8.9 (2013): e74857.

16. Gao, Junling, et al. "Transplantation of primed human fetal neural stem cells improves cognitive function in rats after traumatic brain injury." Experimental neurology 201.2 (2006): 281-292.

17. Riess, Peter, et al. "Transplanted neural stem cells survive, differentiate, and improve neurological motor function after experimental traumatic brain injury." Neurosurgery 51.4 (2002): 1043-1054.

18. Bulte, Jeff WM. "In vivo MRI cell tracking: clinical studies." AJR. American journal of roentgenology 193.2 (2009): 314.

19. Gutova, Margarita, et al. "Magnetic resonance imaging tracking of ferumoxytol-labeled human neural stem cells: studies leading to clinical use." Stem cells translational medicine 2.10 (2013): 766.

20. Guzman, Raphael, et al. "Long-term monitoring of transplanted human neural stem cells in developmental and pathological contexts with MRI." Proceedings of the National Academy of Sciences 104.24 (2007): 10211-10216.

21. Ruiz‐Cabello, Jesús, et al. "In vivo “hot spot” MR imaging of neural stem cells using fluorinated nanoparticles." Magnetic Resonance in Medicine 60.6 (2008): 1506-1511.

22. Boehm-Sturm, Philipp, et al. "In vivo tracking of human neural stem cells with 19F magnetic resonance imaging." PloS one 6.12 (2011): e29040.

23. Bernsen, Monique R., et al. "Labelling of mammalian cells for visualisation by MRI." European radiology 20.2 (2010): 255-274.

24. Poste, George, and Isaiah J. Fidler. "The pathogenesis of cancer metastasis." Nature 283.5743 (1980): 139-146.

25. Weis, Christian, et al. "Labeling of cancer cells with magnetic nanoparticles for magnetic resonance imaging." Magnetic Resonance in Medicine 71.5 (2014): 1896-1905.

26. Heyn, Chris, et al. "In vivo MRI of cancer cell fate at the single‐cell level in a mouse model of breast cancer metastasis to the brain." Magnetic resonance in medicine 56.5 (2006): 1001-1010.

27. Hochachka, P. W., et al. "Going malignant: the hypoxia‐cancer connection in the prostate." Bioessays 24.8 (2002): 749-757.
28. Höckel, Michael, et al. "Association between tumor hypoxia and malignant progression in advanced cancer of the uterine cervix." Cancer research 56.19 (1996): 4509-4515.

29. Bergers, Gabriele, and Laura E. Benjamin. "Tumorigenesis and the angiogenic switch." Nature Reviews Cancer 3.6 (2003): 401-410.

30. Sutherland, Robert, et al. "Spheroids in cancer research." Cancer Research 41.7 (1981): 2980-2984.

31. Hirschhaeuser, Franziska, et al. "Multicellular tumor spheroids: an underestimated tool is catching up again." Journal of biotechnology 148.1 (2010): 3-15.

32. Hood, Maureen N., et al. "Chemical shift: the artifact and clinical tool revisited." Radiographics 19.2 (1999): 357-371.

33. Kodibagkar, Vikram D., et al. "Proton imaging of siloxanes to map tissue oxygenation levels (PISTOL): a tool for quantitative tissue oximetry." NMR in biomedicine 21.8 (2008): 899-907.

34. Auksorius, Egidijus, et al. "Dual-modality fluorescence and full-field optical coherence microscopy for biomedical imaging applications." Biomedical optics express 3.3 (2012): 661-666.

35. He, Xiaoxiao, et al. "Near-infrared fluorescent nanoprobes for cancer molecular imaging: status and challenges." Trends in molecular medicine 16.12 (2010): 574-583.

36. Tsien, Roger Y., and Alan Waggoner. "Fluorophores for confocal microscopy." Handbook of biological confocal microscopy. Springer US, 1995. 267-279.

37. O'Hanlon, Claire E., et al. "NIR-labeled perfluoropolyether nanoemulsions for drug delivery and imaging." Journal of fluorine chemistry 137 (2012): 27-33.

38. Davies, J. T. "A quantitative kinetic theory of emulsion type, I. Physical chemistry of the emulsifying agent." Gas/Liquid and Liquid/Liquid Interface. Proceedings of the International Congress of Surface Activity. 1957.

39. Mahdi Jafari, Seid, Yinghe He, and Bhesh Bhandari. "Nano-emulsion production by sonication and microfluidization—a comparison." International Journal of Food Properties 9.3 (2006): 475-485.

40. Bhirde, Ashwinkumar, et al. "Nanoparticles for cell labeling." Nanoscale 3.1 (2011): 142-153.

41. Smith, Philip J., et al. "Cellular entry of nanoparticles via serum sensitive clathrin-mediated endocytosis, and plasma membrane permeabilization." International journal of nanomedicine 7 (2012): 2045.

42. Amsalem, Yoram, et al. "Iron-oxide labeling and outcome of transplanted mesenchymal stem cells in the infarcted myocardium." Circulation 116.11 suppl (2007): I-38.

43. Arbab, Ali S., et al. "Characterization of biophysical and metabolic properties of cells labeled with superparamagnetic iron oxide nanoparticles and transfection agent for cellular MR imaging 1." Radiology 229.3 (2003): 838-846.

44. Reubinoff, Benjamin E., et al. "Neural progenitors from human embryonic stem cells." Nature biotechnology 19.12 (2001): 1134-1140.

45. Gage, Fred H. "Mammalian neural stem cells." Science 287.5457 (2000): 1433-1438.

46. Yuhas, John M., et al. "A simplified method for production and growth of multicellular tumor spheroids." Cancer research 37.10 (1977): 3639-3643.

47. Zhao D, Jiang L, Mason RP. Measuring changes in tumor oxygenation. Methods Enzymol 2004; 386: 378–418.

48. Kodibagkar, Vikram D., et al. "Novel 1H NMR approach to quantitative tissue oximetry using hexamethyldisiloxane." Magnetic resonance in medicine 55.4 (2006): 743-748.

49. Schenck, John F. "The role of magnetic susceptibility in magnetic resonance imaging: MRI magnetic compatibility of the first and second kinds." Medical physics 23.6 (1996): 815-850.

50. Weiskopf, Nikolaus, et al. "Optimal EPI parameters for reduction of susceptibility-induced BOLD sensitivity losses: a whole-brain analysis at 3 T and 1.5 T." Neuroimage 33.2 (2006): 493-504.

51. Brateman, Libby. "Chemical shift imaging: a review." American Journal of Roentgenology 146.5 (1986): 971-980

52. Caravan, Peter. "Strategies for increasing the sensitivity of gadolinium based MRI contrast agents." Chemical Society Reviews 35.6 (2006): 512-523.

53. Shapiro, Erik M., et al. "MRI detection of single particles for cellular imaging." Proceedings of the National Academy of Sciences of the United States of America 101.30 (2004): 10901-10906.

54. Shapiro, Erik M., et al. "In vivo detection of single cells by MRI." Magnetic Resonance in Medicine 55.2 (2006): 242-249.

55. Neuberger, Tobias, et al. "Superparamagnetic nanoparticles for biomedical applications: possibilities and limitations of a new drug delivery system." Journal of Magnetism and Magnetic Materials 293.1 (2005): 483-496.

56. Babcock, Evelyn E., et al. "Edge artifacts in MR images: chemical shift effect." Journal of computer assisted tomography 9.2 (1985): 252-257.

57. Dwyer, Andrew J., Richard H. Knop, and D. I. Hoult. "Frequency shift artifacts in MR imaging." Journal of computer assisted tomography 9.1 (1985): 16-18.

58. Arbab, Ali S., et al. "Efficient magnetic cell labeling with protamine sulfate complexed to ferumoxides for cellular MRI." Blood 104.4 (2004): 1217-1223.